CrossMark

U-Pb geochronology on zircon and columbite-group minerals of the Cap de Creus pegmatites, NE Spain

Marieke Van Lichtervelde[1] · Alexis Grand'Homme[2] · Michel de Saint-Blanquat[1] ·
Philippe Olivier[1] · Axel Gerdes[3] · Jean-Louis Paquette[4] · Joan Carles Melgarejo[5] ·
Elena Druguet[6] · Pura Alfonso[7]

Abstract The Cap de Creus granitic pegmatites in the eastern Catalan Pyrenees were dated using *in situ* U-Pb geochronology by laser ablation ICP-MS on zircon and columbite-group minerals (CGM), which are present in the different types of pegmatites from type I (K-feldspar pegmatites, least evolved) to type IV (albite pegmatites, most evolved) and therefore allow dating the different pegmatitic pulses. In a type III pegmatite where zircon and CGM are co-genetically associated in the same sample, both minerals were dated using zircon and tantalite reference materials, respectively, to avoid laser-induced matrix-dependent fractionation. In one sample, xenotime genetically associated with zircon was also dated. Two ages were obtained for type I and three ages for type III pegmatites. Three of these 5 ages range from 296.2 ± 2.5 to 301.9 ± 3.8 Ma and are allocated to the primary magmatic stage of crystallization and therefore to the emplacement event. Two younger ages (290.5 ± 2.5 and 292.9 ± 2.9 Ma) obtained on secondary zircon and xenotime, respectively, are interpreted as late post-solidus hydrothermal remobilization. There is no age difference between type I and type III pegmatites. The mean 299 Ma primary magmatic age allows the main late Carboniferous deformation event to be dated and is also synchronous with other peraluminous and calc-alkaline granites in the Pyrenees. However, the youngest ages around 292 Ma imply that tectonics was still active in Early Permian times in the Cap de Creus area.

✉ Marieke Van Lichtervelde
marieke.vanlichtervelde@get.omp.eu

[1] Géosciences Environnement Toulouse, Université de Toulouse, CNES, CNRS, IRD, UPS, 14 avenue Edouard Belin, 31400 Toulouse, France

[2] ISTerre, Université Grenoble, 1381 Rue de la Piscine, BP 53, 38041 Grenoble, France

[3] Department of Geosciences, Petrology and Geochemistry, Goethe-University Frankfurt, Altenhoeferallee 1, 60438 Frankfurt am Main, Germany

[4] UMR 6524 Laboratoire Magmas et Volcans, Clermont Université, Université Blaise Pascal, CNRS, IRD, BP 10448, 63000 Clermont-Ferrand, France

[5] Departament de Cristal·lografia, Mineralogia i Dipòsits Minerals, Universitat de Barcelona, C/ Martí i Franquès s/n, 08028 Barcelona, Catalonia, Spain

[6] Departament de Geologia, Universitat Autònoma de Barcelona, 08193 Bellaterra (Barcelona), Catalonia, Spain

[7] Departament d'Enginyeria Minera i Recursos Naturals, Escola Politècnica Superior d'Enginyeria de Manresa-UPC, Avinguda Bases de Manresa, 61–73, 08240 Manresa, Spain

Introduction

The Cap de Creus peninsula (NE Spain) in the easternmost end of the Pyrenean Axial Zone is a remarkable center of interest for geologists because of its well-exposed outcrops that reveal a complex tectonic, metamorphic and magmatic history. Several episodes of deformation and regional metamorphism are accompanied by calc-alkaline and peraluminous magmatism and affected a late Proterozoic series of metasediments and metavolcanics during the Variscan orogeny. An important group of mineralized granitic pegmatites is associated with these tectonic events.

The study of granitic pegmatites in Europe is gaining interest because these highly fractionated rocks are important sources of industrial minerals and strategic metals such as Li

and the high field strength elements Nb-Ta and Sn (Linnen et al. 2012). In Europe rare-element granitic pegmatites are abundant in the Variscan terrains (French Massif Central, Iberian Massif, Moldanubian domains of Czech Republic, Slovakia and Germany). The Cap de Creus area is one of these fields.

Studies on the geology of Cap de Creus essentially dealt with structural aspects and tectonic interpretations of the Variscan orogeny (Carreras 1975, 2001; Carreras and Druguet 1994, 2013; Druguet and Hutton 1998; Druguet 2001; Fusseis et al. 2006) and the petrology of the peraluminous pegmatites (Corbella and Melgarejo 1993; Alfonso et al. 1995, 2003; Alfonso and Melgarejo 2008). Apart from the recent study by Druguet et al. (2014) that dated a granodiorite and a quartz diorite intrusion, geochronology of the Variscan in Cap de Creus was only indirectly inferred from other studies in the Eastern Pyrenees (e.g., Aguilar et al. 2014).

The peraluminous pegmatite swarm that crops out in the Cap de Creus area consists of different types of pegmatites, ranging from type I (K-feldspar pegmatites, least evolved) to type IV (albite pegmatites, most evolved), distributed along zones of increasing intensity of the deformation and metamorphic grade. Consequently, dating the Cap de Creus pegmatites could better frame the geological history of the Variscan orogeny in the Pyrenees and particularly could help to place a timeline on the succession of tectonic events. The pegmatites contain U-bearing accessory minerals such as zircon, xenotime and columbite-group minerals (CGM). The aim of our study is to date these minerals in order to constrain the pegmatite emplacement. Age correlations with published geochronological data on peraluminous granite and migmatitic rocks from the area may also help to establish a model for the anatectic *versus* granitic origin of the mineralized pegmatites during the Variscan orogeny.

Columbite-tantalite is well suited for U-Pb age determination of pegmatite emplacement. It generally contains around 500 ppm U, but values up to 10,000 ppm are not uncommon, and it accommodates low common Pb. Solid state U-Pb diffusion is also thought to be minor in CGM (Romer and Wright 1992). Columbite-tantalite is a common primary magmatic mineral phase in pegmatites, and its refractory nature makes it resistant to hydrothermal alteration and weathering. Large crystals several hundred microns in size allow detailed characterization of their internal textural features, thus permitting precise location of the ablation laser spots with respect to possible late precipitation phases, metamict zones and U-bearing inclusions. Columbite-tantalite is a good alternative to date pegmatites where zircon is too U-rich and highly metamict. The present study gives ages from both zircon and CGM associated together in the same samples, using a thorough sorting out of metamict grains.

Geological setting

General features

The study area is located in the Northern Cap de Creus peninsula (Fig. 1). It consists of metasedimentary rocks (metagreywackes, metapelites, rare quartzites) with minor metavolcanic intercalations. The protolith of this sequence is referred to as the Cadaqués series (Navidad and Carreras 1995) and is considered Neoproterozoic in age. During the Variscan, the rocks of the Cadaqués series were affected by polyphase deformation with three main deformation episodes (D1, D2, D3; Druguet 2001), the two first ones occurred during the prograde LP-HT regional metamorphism and the last one during late shearing events under retrograde conditions. Metasediments show a gradient from the chlorite-muscovite zone in the south (out of the map in Fig. 1) to the sillimanite-K feldspar zone in the north. Locally, migmatites were formed in the sillimanite-K feldspar zone (Druguet et al. 1997). High to medium grade schists in the northern part of the area are extensively intruded by pegmatite (Fig. 1; Carreras and Druguet 1994; Bons et al. 2004).

The oldest deformation in the area (D1) led to the development of a first continuous and penetrative N-S trending bedding-parallel schistosity (Sl) in the metasediments prior to the metamorphic climax. Later intense and inhomogeneous D2 deformation led to folding and shearing of S1 with upright or steeply inclined axial surfaces which trend approximately NE-SW in less deformed areas and E-W in more deformed areas. Parallel with the increase of metamorphic grade, the intensity of the D2 event increases from south to north, where a 200 m thick E–W trending zone of high strain is observed and S1 is transposed into a steeply dipping composite S1/S2 foliation with a few relics of tight to isoclinal D2 folds (Druguet and Carreras 2006). L2 lineations are generally steeply plunging towards the NW. D2 structures formed around peak metamorphic conditions, as shown by the presence of synkinematic sillimanite and by partial melting of metasediments. A third episode of deformation of unknown age occurred under retrograde (greenschist facies) metamorphic conditions and was characterized by strain localization that gave rise to a network of D3 shear bands with predominantly reverse-dextral movement. These form the classical Cap de Creus shear zones and mylonites which overprint and therefore postdate all the preexisting structures (Carreras 2001). Unambiguous field relationships show that pegmatites intruded after D1 and before D3, that is more or less contemporaneously with D2 (Fig. 2).

Published geochronological data of Cap de Creus

The Cadaqués metasedimentary series, although not directly dated, is inferred to be older than the El Port de la Selva gneiss
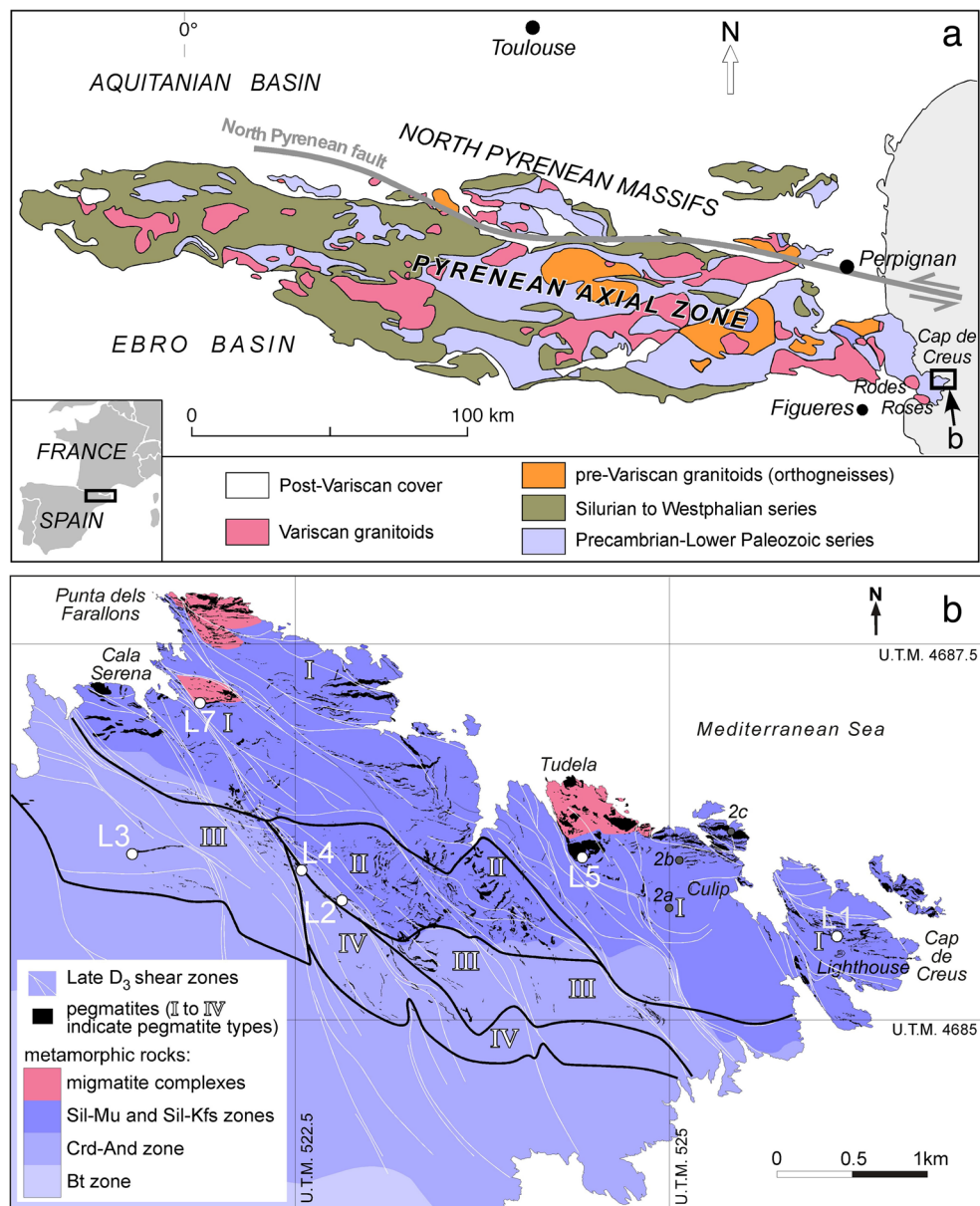
Fig. 1 **a** Geological map of the central and eastern Pyrenean Axial Zone (modified from Druguet et al. 2014). **b** Geological map of the north Cap de Creus area, showing the distribution of the four pegmatite types (modified from Corbella and Melgarejo 1993) within the three metamorphic zones (Sil-Mu: sillimanite-muscovite; Sil-Kfs: sillimanite-K-feldspar; Crd-And: cordierite-andalusite; Bt: biotite; the chlorite-muscovite zone is further to the south, out of the map). The main shear zones of the mylonite belt and the sampled pegmatite localities are also shown. Labels 2a, 2b and 2c correspond to the locations of photographs in Fig. 2. Modified from Druguet and Carreras (2006)

(located about 5 km west of the Punta dels Farallons, Fig. 1b), whose igneous precursor intruded the metasedimentary series and was dated at 553.0 ± 4.4 Ma (Castiñeiras et al. 2008). Zircons from the Tudela migmatite (northern part of the Cap de Creus, Fig. 1b) yield inherited ages from the Precambrian protolith, with two main age clusters at *c.* 2.9–2.2 Ga and *c.* 730–542 Ma (Druguet et al. 2014). However, based on field structural relationships, Druguet et al. (2014) interpret that the migmatization event was synchronous with the emplacement of a syntectonic quartz diorite from

the Tudela migmatitic complex dated at 298.8 ± 3.8 Ma by these authors. The western and southern granitoid stocks, known as Rodes and Roses stocks respectively (Fig. 1a), consist of granodiorite and tonalite and were emplaced within lower-grade rocks at 290.8 ± 2.9 Ma (Druguet et al. 2014). For further geochronological data in the Pyrenees, the reader can refer to Laumonier et al. (2004); Cocherie et al. (2005); Casas et al. (2010); Liesa et al. (2011), Aguilar et al. (2014), Denèle et al. (2014) and Casas et al. (2015).
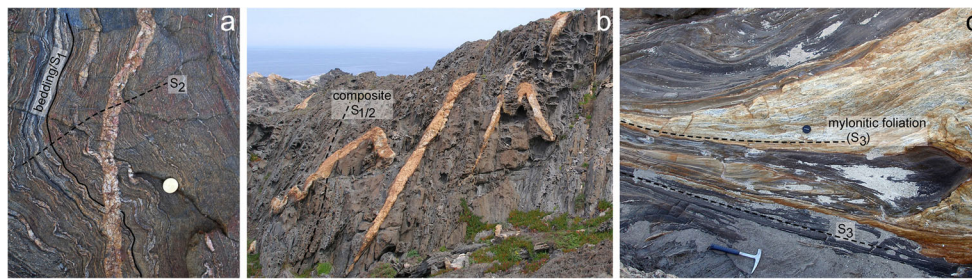
Fig. 2 Field photographs showing the relationships between pegmatite dykes and deformation phases (see location on Fig. 1). **a** Pegmatitic vein crosscutting bedding/S1 and being slightly folded by D2. Zone of low D2 strain south of Puig de Culip. **b** Syntectonic pegmatite dykes are folded by D2 in a zone of strong D2 strain, as shown by a penetrative composite S1/S2 fabric. North of Puig de Culip. **c** Mylonitic foliation (S3) affecting schists and a pegmatite body at the margin of a late dextral zone. NW Cala Culip

Pegmatites

Four types of peraluminous, lithium-cesium-tantalum-family pegmatites (after the classification of Černỳ and Ercit 2005) were distinguished among the ~400 bodies that crop out in Cap de Creus. This distinction was made on mineralogical and textural criteria (Corbella and Melgarejo 1993). Type I pegmatites are barren with graphic textures and a relatively simple concentric structure roughly consisting of border, first intermediate and second intermediate zones; in addition to biotite and muscovite, peraluminous minerals as cordierite, sillimanite, andalusite, almandine and schorl are very common in all these zones. Xenotime is associated with zircon in this pegmatite type. Type II pegmatites are transitional with the most evolved pegmatites; the main differences with type I are the occurrence of a well developed quartz core and the existence of late albite units. In addition to the above mentioned peraluminous minerals, these pegmatites may contain chrysoberyl, gahnite, green beryl, Ca-Fe-Mn-Mg-phosphates and some Be- and Al-phosphates. Nb-rich minerals of the columbite group are scarce in all units as well as wolframite, Sc-rich rutile and uraninite. The internal structure of type III pegmatites is more complex with large quartz cores and well developed albite and quartz-muscovite replacement units. Biotite is absent and schorl is scarce; garnet is enriched in the spessartine component. White beryl, montebrasite and Li-Fe-phosphates are common in the second intermediate unit and in the albite or quartz-muscovite replacement veins, as well as Ta-rich minerals of the columbite group, cassiterite and uraninite. Type IV pegmatites are the most evolved in the field. In addition to the above mentioned units, they may also contain late Al-phosphate veins. Beryl or chrysoberyl, montebrasite and Li-Mn phosphates are common. Ore minerals consist of Ta-Mn rich members of the columbite group, as well as cassiterite, tapiolite and aeschynite. Following the classical pegmatite classification (Černỳ and Ercit 2005), type II pegmatites belong to the beryl-columbite subtype, type III belong to the beryl-columbite-phosphate subtype, and type IV belong to the albite subtype. Type I pegmatites are nearly sterile and may be considered as pegmatitic granite rather than pegmatite *sensu stricto*.

The four types of pegmatites occupy different zones parallel to the tectono-metamorphic zoning (Fig. 1): types I and II occur in high-grade and high-D2 strain rocks of the migmatite and sillimanite-muscovite zones that lie along the northern coast, whereas types III and IV occur in medium-grade metamorphic rocks of the cordierite-andalusite zone to the south. The size and frequency of the pegmatite bodies decrease from type I to type IV (Corbella and Melgarejo 1993): along the northern coast, large stocks of pegmatitic granite may reach a length of several hundreds of meters and a width of more than 50 m, whereas 2 km further to the southwest, only a few bodies outcrop with a maximum length of 30 m.

In general, pegmatite dykes follow the main S2 foliation, and are locally affected by late shearing. Some dykes that were emplaced oblique to S2 foliation are affected by ductile folding.

Sampling and analytical procedure

Rock samples were collected on six dykes representative of type I, III and IV pegmatites (Fig. 1), but only two locations (L3 and L7) were relevant for dating. Polished sections and thin sections were prepared for mineralogical description and investigation of the mineral textures to determine the primary magmatic *versus* secondary nature of the dated minerals. In samples where zircon suitable for dating was observed, a larger sample volume was crushed and zircon was separated using a standard separation procedure: 1) gravity separation using either a shaking table or a gold pan; 2) heavy liquid separation using tetrabromo-ethane; 3) magnetic separation to eliminate the metamict zircon grains; 4) heavy liquid separation using metyleniodide. Thirty to 40 separated grains per sample were mounted in lines in epoxy resin blocks that were subsequently polished. In L7 sample, xenotime occurs in direct contact with zircon and was therefore dated together with it. Because of their coarse-grained habit, CGM crystals were directly dated on the polished sections.

Back-scattered electrons (BSE) images were taken for each zircon and CGM grain, and crack- and inclusion-free domains were selected for the laser spots. In sample L7 where zircon shows complex textures, additional cathodoluminescence (CL) images were taken in order to highlight the metamict parts of the altered domains.

Quantitative chemical analyses were carried out with a Cameca SX50 electron probe micro-analyzer (EPMA) using a 15 kV accelerating voltage, 20 nA beam current, 1 μm beam diameter, 10 s and 5 s acquisition times on peak and background respectively, natural and synthetic calibrant materials (Ta, Nb, and W metals, cassiterite, zircon, hematite, wollastonite, $MnTiO_3$, $ScPO_4$, UO_2, ThO_2, Pb glass), and ZAF correction procedures.

Uranium-lead dating of CGM, xenotime and zircon was carried out in-situ at the Goethe University of Frankfurt (GUF) using a slightly modified method as the one previously described in Gerdes and Zeh (2006, 2009) and Zeh and Gerdes (2012). Thermo-Scientific Element II sector field ICP-MS was coupled to a Resolution M-50 (Resonetics) 193 nm ArF Excimer laser (CompexPro 102, Coherent) equipped with two-volume ablation cell (Laurin Technic, Australia). Samples were ablated in a helium atmosphere (0.6 l/min) and mixed in the ablation funnel with 0.7 l/min argon and 0.02 l/min nitrogen. Signal strength at the ICP-MS was tuned for maximum sensitivity while keeping oxide formation below 1 %. The laser was fired with 5.5 Hz at a fluence of about 2–3 J cm^{-2}. This yielded with the above configuration at a spot size of 30 μm and depth penetration of 0.6 μm s^{-1} a sensitivity of 11,000–13,000 cps/μg g^{-1} for ^{238}U. Raw data were corrected offline for background signal, common Pb, laser induced elemental fractionation, instrumental mass discrimination, and time-dependent elemental fractionation of Pb/U using an in-house MS Excel© spreadsheet program (Gerdes and Zeh 2006, 2009).

Laser-induced elemental fractionation and instrumental mass discrimination were corrected by normalization to the reference zircon GJ-1 (0.0982 ± 0.0003; ID-TIMS GUF value). Repeated analyses of the reference zircon Plesovice and 91,500 (Slama et al. 2008; Wiedenbeck et al. 2005) during the same analytical session yielded an accuracy of better 1 % and a reproducibility of <2 % (2 SD). The same applies to monazite run as secondary standards normalized to GJ-1 using the same analytical setting and tune parameter except of the spot size: 15 μm relative to 33 μm for GJ-1. Repeated analyses ($n = 9$) of the reference monazite Manangotry and Moacir (Horstwood et al. 2003; Gonçalves et al. 2016) yielded an accuracy of around ~1 % and reproducibility of 2–3 % (2 SD). This is in line with previous studies at GUF that have shown that LA-SF-ICP-MS with non-matrix matched standardization can yield precise and accurate U–Pb ages for different phosphate minerals (e.g., Meyer et al. 2006; Millonig et al. 2013 and references therein). Thus no correction for

phosphate matrix have been applied for xenotime analysis. However, in case of CGM the Coltan 139 (Gäbler et al. 2011) was used as matrix matched standard. More details on the operating conditions and instrument settings are given in Gerdes and Zeh (2006, 2009) and in data Tables 1 and 2. All uncertainties are reported at the 2sigma level.

One zircon age was duplicated at the Laboratoire Magmas et Volcans of Clermont-Ferrand, equipped with an Excimer 193 nm laser coupled to a quadrupole Agilent 7500 ICP-MS, using zircon GJ-1 as reference material (analytical techniques described in Paquette et al. 2014). However, the Thermo-Scientific Element II sector field ICP-MS in Frankfurt is more adapted to Hercynian ages since it has a better precision on the U/Pb ratios and its higher sensitivity allows better correction for common Pb. For CGM ages, an external manganotantalite crystal (Coltan 139; Gäbler et al. 2011) from Madagascar was used to correct for matrix-dependent U/Pb elementary fractionation. This reference was used to date CGM from African pegmatites with the goal to fingerprint illegally mined coltan (Melcher et al. 2008, 2015). The Coltan 139 reference is a large manganotantalite crystal that is isotopically and chemically homogeneous at the micrometer scale, has a U concentration of about 1600 ppm and low common Pb (Gäbler et al. 2011). It displays an intercept age of 505.6 ± 3.4 Ma obtained by LA-ICP-MS and verified by ID-TIMS. Where necessary, the various textural domains of zircon and CGM were dated, and most crystals were measured in both core and rim for comparison. Concordia diagrams were plotted using Isoplot 3.7 (Ludwig 2008).

Results

Dated pegmatites and minerals

Six pegmatite dykes (Fig. 1) were studied but only two of them displayed CGM, xenotime and/or zircon crystals that were suitable for dating. Textural and chemical features of CGM and zircon were studied in all pegmatites where they were observed. In type I pegmatites L1 and L5, no CGM was found and most zircon crystals were too small (c. 10 μm) to be dated. In type II pegmatite L2, zircon crystals were too small and altered to be dated, but CGM displayed a few prismatic crystals that could be dated in Clermont-Ferrand. However, standardization on zircon lead us to exclude those CGM ages. In type IV pegmatite L4, the zircon crystals were larger (c. 100 μm), but they were highly metamict and rich in uraninite inclusions, and displayed uninterpretable ages due to loss of radiogenic Pb on one hand and entry of common Pb on the other. Although CGM are also common in type IV pegmatites, they are generally associated with the aplitic albite units and their crystals were too fine-grained to be dated. The two dated

Table 1   Age data obtained by LA-ICP-MS for pegmatite L3

Spot	$^{207}Pb^{a}$ (cps)	U^{b} (ppm)	Pb^{b} (ppm)	$\frac{Th}{U}^{b}$	$^{206}Pbc^{c}$ (%)	$\frac{^{206}Pb}{^{238}U}^{d}$	±2σ (%)	$\frac{^{207}Pb}{^{235}U}^{d}$	±2σ (%)	$\frac{^{207}Pb}{^{206}Pb}^{d}$	±2σ (%)	rho^{e}	$\frac{^{206}Pb}{^{238}U}$	±2σ (Ma)	$\frac{^{207}Pb}{^{235}U}$	±2σ (Ma)	$\frac{^{207}Pb}{^{206}Pb}$	±2σ (Ma)	conc.^{f} (%)
Tantalite																			
A07	5690	103	4.3	0.0027	1.70	0.04343	2.2	0.30760	4.1	0.05136	3.4	0.54	274	6	272	10	257	79	107
A08	7288	113	4.4	0.0024	1.70	0.03862	2.2	0.27910	3.7	0.05241	3.0	0.60	244	5	250	8	304	68	80
A09	16,152	192	7.2	0.0018	5.47	0.03468	3.4	0.24800	6.7	0.05187	5.8	0.51	220	7	225	14	280	132	79
A10	8822	134	4.9	0.0027	1.81	0.03565	2.4	0.26040	3.8	0.05297	3.0	0.62	226	5	235	8	327	68	69
A11	8375	125	4.8	0.0026	1.78	0.03868	3.3	0.27900	4.8	0.0523	3.5	0.69	245	8	250	11	299	79	82
A12	8537	175	7.1	0.0038	10.41	0.03355	3.1	0.24260	9.4	0.05245	8.9	0.33	213	6	221	19	305	203	70
A13	7118	290	11.4	0.0034	1.84	0.04149	3.1	0.29920	4.8	0.05229	3.6	0.65	262	8	266	11	298	83	88
A14	7136	246	10.2	0.0028	3.02	0.04184	2.7	0.30100	5.3	0.05218	4.6	0.50	264	7	267	13	293	106	90
A15	8785	278	11.6	0.0026	1.67	0.04065	2.0	0.29170	3.1	0.05203	2.3	0.65	257	5	260	7	287	53	90
A16	4718	254	8.0	0.0016	1.20	0.03363	2.3	0.24170	3.7	0.05211	2.9	0.61	213	5	220	7	290	67	73
A17	7419	321	11.3	0.0022	1.10	0.03736	2.5	0.26720	3.4	0.05188	2.3	0.74	236	6	240	7	280	52	84
A18	4377	159	7.4	0.0034	1.90	0.04884	2.9	0.35570	4.5	0.05282	3.4	0.64	307	9	309	12	321	78	96
A19	3640	164	6.7	0.0017	0.54	0.04415	2.9	0.31810	4.5	0.05226	3.5	0.63	278	8	280	11	297	81	94
A20	7780	369	15.0	0.0021	1.21	0.04413	2.1	0.31740	3.8	0.05216	3.2	0.56	278	6	280	9	293	72	95
A21	1461	61	2.3	0.0033	1.59	0.04022	3.9	0.29520	5.7	0.05323	4.2	0.68	254	10	263	13	339	94	75
A22	3824	152	4.1	0.0024	1.89	0.02517	2.9	0.18150	5.1	0.05230	4.2	0.57	160	5	169	8	299	96	54
A23	2982	75	2.1	0.0017	0.96	0.02970	2.4	0.21240	3.8	0.05186	2.9	0.63	189	4	196	7	279	67	68
A24	3154	63	1.6	0.0018	2.11	0.02575	3.3	0.18670	6.1	0.05258	5.1	0.55	164	5	174	10	311	117	53
A25	3481	70	1.9	0.0017	1.46	0.02851	2.8	0.20440	4.8	0.05200	3.9	0.58	181	5	189	8	285	89	63
A26	3804	79	2.8	0.0018	2.06	0.03781	2.8	0.27130	4.8	0.05205	4.0	0.57	239	7	244	11	288	91	83
A27	4715	119	4.9	0.0027	2.35	0.03798	2.4	0.27530	6.0	0.05257	5.4	0.41	240	6	247	13	310	124	77
A28	2248	102	2.9	0.0020	0.79	0.03085	2.4	0.22030	4.6	0.05179	4.0	0.52	196	5	202	9	276	91	71
A29	2157	73	2.4	0.0028	2.78	0.03158	2.4	0.23250	4.8	0.05339	4.1	0.50	200	5	212	9	345	93	58
A30	1893	96	3.1	0.0015	0.32	0.03531	2.3	0.25200	3.9	0.05177	3.1	0.60	224	5	228	8	275	70	81
A31	2608	111	5.1	0.0018	1.63	0.04864	2.2	0.35080	4.5	0.05231	3.9	0.49	306	7	305	12	299	89	102
A32	3339	98	4.7	0.0013	1.09	0.04842	2.5	0.35020	5.5	0.05245	4.9	0.45	305	7	305	15	305	112	100
A39	3711	129	6.0	0.0020	1.86	0.04851	2.7	0.34840	4.9	0.05210	4.1	0.56	305	8	304	13	290	93	105
A40	10,111	231	10.7	0.0014	2.88	0.04287	2.8	0.30710	5.3	0.05196	4.5	0.52	271	7	272	13	283	103	95
A41	4745	216	9.4	0.0016	0.44	0.04710	2.4	0.33900	3.7	0.05220	2.9	0.63	297	7	296	10	294	66	101
A42	3236	142	5.8	0.0025	1.55	0.04300	2.6	0.31110	4.7	0.05248	3.9	0.56	271	7	275	11	306	88	89
A43	36,706	272	19.8	0.0061	11.77	0.04034	3.1	0.29010	6.9	0.05217	6.1	0.46	255	8	259	16	293	140	87
A44	3269	129	5.6	0.0021	1.08	0.04625	2.8	0.33310	4.2	0.05225	3.1	0.68	291	8	292	11	296	70	98
A45	7872	253	9.1	0.0025	1.66	0.03398	3.1	0.24520	5.1	0.05233	4.0	0.62	215	7	223	10	300	91	72
A46	7154	209	8.6	0.0024	1.99	0.04035	2.3	0.29140	4.3	0.05238	3.7	0.53	255	6	260	10	302	84	84
Zircon																			
A47	48,837	7979	247	0.0054	1.04	0.03334	2.1	0.24040	2.8	0.05230	1.9	0.73	211	4	219	6	299	44	71
A48	162,591	30,792	409	0.0046	2.43	0.01285	4.3	0.09108	5.0	0.05139	2.5	0.86	82	4	89	4	258	58	32
A49	36,135	4707	140	0.0040	0.88	0.03197	2.6	0.22970	3.1	0.05211	1.8	0.82	203	5	210	6	290	41	70

Table 1 (continued)

Spot	^{207}Pb[a] (cps)	U[b] (ppm)	Pb[b] (ppm)	$\frac{\text{Th}}{\text{U}}$[b]	^{206}Pbc[c] (%)	$\frac{^{206}\text{Pb}}{^{238}\text{U}}$[d]	±2σ (%)	$\frac{^{207}\text{Pb}}{^{235}\text{U}}$[d]	±2σ (%)	$\frac{^{207}\text{Pb}}{^{206}\text{Pb}}$[d]	±2σ (%)	rho[e]	$\frac{^{206}\text{Pb}}{^{238}\text{U}}$	±2σ (Ma)	$\frac{^{207}\text{Pb}}{^{235}\text{U}}$	±2σ (Ma)	$\frac{^{207}\text{Pb}}{^{206}\text{Pb}}$	±2σ (Ma)	conc[f] (%)
A50	20,879	3170	53	0.0034	2.57	0.01671	4.2	0.11950	5.5	0.05187	3.5	0.77	107	4	115	6	280	81	38
A51	38,483	9427	113	0.0052	2.29	0.01226	3.5	0.08769	4.7	0.05186	3.1	0.74	79	3	85	4	279	72	28
A52	63,246	9761	279	0.0033	0.12	0.03127	1.9	0.22520	2.1	0.05224	0.8	0.92	199	4	206	4	296	18	67
A53	55,134	8151	220	0.0024	0.28	0.02938	2.6	0.20980	2.8	0.05177	1.0	0.93	187	5	193	5	275	23	68
A54	92,367	12,086	385	0.0023	0.05	0.03489	2.2	0.25140	2.3	0.05226	0.7	0.96	221	5	228	5	297	16	75
A55	61,176	6292	249	0.0021	0.36	0.04303	2.3	0.30960	2.6	0.05218	1.1	0.91	272	6	274	6	293	25	93
A56	34,405	5076	90	0.0143	3.07	0.01775	2.1	0.12870	4.3	0.05257	3.7	0.49	113	2	123	5	310	85	37
A57	59,118	12,247	196	0.0034	1.98	0.01691	3.3	0.11970	4.5	0.05132	3.0	0.74	108	4	115	5	255	70	42
A58	60,500	7065	251	0.0032	0.10	0.03883	2.1	0.28330	2.3	0.05292	0.9	0.92	246	5	253	5	326	21	75
A59	104,102	10,398	440	0.0019	0.07	0.04632	1.8	0.33460	1.9	0.05239	0.6	0.94	292	5	293	5	303	15	96
A60	47,786	12,713	105	0.0023	0.55	0.00884	3.2	0.06342	3.4	0.05206	1.3	0.93	57	2	62	2	288	29	20
A61	42,443	5581	163	0.0038	1.42	0.03121	1.9	0.22670	3.0	0.05268	2.3	0.64	198	4	207	6	315	52	63
A62	68,022	10,627	191	0.0078	3.19	0.01811	3.1	0.13110	4.9	0.05252	3.8	0.62	116	4	125	6	308	88	38
A63	56,045	6135	227	0.0026	0.31	0.04046	2.3	0.28990	2.5	0.05196	0.9	0.93	256	6	258	6	284	21	90
A64	135,655	16,552	667	0.0026	0.30	0.04390	2.3	0.31910	2.4	0.05271	0.8	0.95	277	6	281	6	316	18	88
A65	82,176	8328	347	0.0017	0.03	0.04573	1.8	0.32790	2.0	0.05200	0.8	0.92	288	5	288	5	285	18	101
A66	165,733	14,988	535	0.0017	1.07	0.03780	2.0	0.27250	2.6	0.05228	1.7	0.76	239	5	245	6	298	39	80
A73	51,895	7507	184	0.0055	0.84	0.02635	2.4	0.18930	2.9	0.05209	1.6	0.84	168	4	176	5	290	36	58
A74	96,940	9990	344	0.0018	0.02	0.03775	1.9	0.27030	2.0	0.05193	0.7	0.93	239	4	243	4	282	16	85
A75	107,160	14,471	582	0.0014	0.09	0.04401	1.8	0.31840	2.0	0.05248	0.8	0.90	278	5	281	5	306	19	91
A76	139,336	15,704	543	0.0025	0.30	0.03760	1.7	0.27290	1.9	0.05264	0.9	0.88	238	4	245	4	313	21	76
A77	50,140	12,242	220	0.0031	0.26	0.01960	2.3	0.14000	2.6	0.05182	1.1	0.91	125	3	133	3	277	25	45
A78	19,184	6149	108	0.0013	0.45	0.01918	3.1	0.13580	3.3	0.05133	1.3	0.93	123	4	129	4	256	29	48
Reference materials																			
Plešovice[g]	17,315	705	36	0.08	0.19	0.05367	1.1	0.39226	0.7	0.05301	1.1	0.79	337	4	336	2	329	26	103
Col139[g]	55,336	1172	90	0.03	1.00	0.08037	5.9	0.63527	5.5	0.05733	0.9	0.81	498	28	499	22	504	20	99
91,500[g]	8160	72	14	0.31	0.52	0.17935	1.7	1.85625	1.6	0.07507	1.2	0.62	1063	17	1066	11	1070	23	99

Spot size =26 μm; depth of crater ~15 μm. ^{206}Pb/^{238}U error is the quadratic additions of the within run precision (2 SE) and the external reproducibility (2 SD) of the reference zircon. ^{207}Pb/^{206}Pb error propagation (^{207}Pb signal dependent) following Gerdes and Zeh (2009). ^{207}Pb/^{235}U error is the quadratic addition of the ^{207}Pb/^{206}Pb and ^{206}Pb/^{238}U uncertainty

[a] Within run background-corrected mean ^{207}Pb signal in cps (counts per second)

[b] U and Pb content and Th/U ratio were calculated relative to GJ-1 reference zircon

[c] Percentage of the common Pb on the ^{206}Pb. b.d. = below detection limit

[d] Corrected for background, within-run Pb/U fractionation (in case of ^{206}Pb/^{238}U) and common Pb using Stacey and Kramers (1975) model Pb composition and subsequently normalised to GJ-1 (ID-TIMS value/measured value); ^{207}Pb/^{235}U calculated using ^{207}Pb/^{206}Pb/(^{238}U/^{206}Pb*1/137.88)

[e] rho is the ^{206}Pb/^{238}U/^{207}Pb/^{235}U error correlation coefficient

[f] Degree of concordance =^{206}Pb/^{238}U age / ^{207}Pb/^{206}Pb age × 100

[g] Accuracy and reproducibilty was checked by repeated analyses (n = 12) of reference zircon Plešovice and 91,500 and columbite 139; data given as mean with 2 standard deviation uncertainties

Table 2 Age data obtained by LA-ICP-MS for pegmatite L7

Grain	207Pb[a] (cps)	U[b] (ppm)	Pb[b] (ppm)	Th[b]/U	206Pbc[c] (%)	206Pb[d]/238U	±2σ (%)	207Pb[d]/235U	±2σ (%)	207Pb[d]/206Pb	±2σ (%)	rho[e]	206Pb/238U (Ma)	±2σ (Ma)	207Pb/235U (Ma)	±2σ (Ma)	207Pb/206Pb (Ma)	±2σ (Ma)	conc.[f] (%)
zr1 primary zircon																			
A06	98,165	11,350	405	0.003	1.3	0.03800	2.8	0.27300	4.4	0.05210	3.4	0.64	240	7	245	10	290	77	83
A07	65,219	8008	326	0.003	0.3	0.04433	2.8	0.32110	3.2	0.05254	1.6	0.88	280	8	283	8	309	35	91
A09	91,517	10,643	438	0.007	1.4	0.04369	2.8	0.31610	4.4	0.05246	3.3	0.65	276	8	279	11	306	76	90
A12	28,197	3693	152	0.001	0.0	0.04519	2.8	0.32380	3.2	0.05197	1.5	0.89	285	8	285	8	284	34	100
A14	64,080	8252	354	0.001	0.2	0.04688	2.7	0.33680	3.0	0.05210	1.3	0.91	295	8	295	8	290	29	102
A16	119,645	11,421	417	0.015	3.8	0.03633	3.0	0.26130	7.4	0.05217	6.7	0.41	230	7	236	16	293	154	79
A19	210,424	11,150	535	0.021	1.7	0.04412	2.6	0.32030	3.7	0.05265	2.6	0.70	278	7	282	9	314	60	89
A21	65,704	8780	371	0.001	0.0	0.04629	2.6	0.33570	2.8	0.05259	1.1	0.93	292	7	294	7	311	24	94
A22	97,380	12,616	513	0.002	0.3	0.04444	2.8	0.32040	3.1	0.05228	1.4	0.90	280	8	282	8	298	32	94
A24	63,963	8751	382	0.001	0.0	0.04783	2.8	0.34600	3.2	0.05247	1.4	0.90	301	8	302	8	306	31	98
A26	38,271	4929	217	0.003	0.3	0.04800	2.5	0.35260	2.9	0.05328	1.6	0.85	302	7	307	8	341	35	89
A31	139,566	14,962	602	0.008	2.0	0.04210	2.8	0.30550	5.1	0.05264	4.3	0.55	266	7	271	12	313	97	85
A32	59,163	5536	255	0.008	2.1	0.04802	2.8	0.34500	5.3	0.05210	4.5	0.53	302	8	301	14	290	103	104
A38	71,407	9289	390	0.002	0.2	0.04599	2.7	0.33190	3.0	0.05234	1.3	0.89	290	8	291	8	300	30	97
A39	112,599	9886	393	0.002	3.7	0.03975	3.3	0.28870	7.6	0.05268	6.9	0.44	251	8	258	17	315	156	80
A40	94,785	10,929	474	0.004	1.2	0.04640	2.8	0.33040	4.1	0.05164	3.0	0.68	292	8	290	10	270	68	108
A41	31,337	4209	179	0.003	0.4	0.04638	2.8	0.33110	3.5	0.05178	2.0	0.81	292	8	290	9	276	46	106
A43	67,728	9108	397	0.001	0.1	0.04784	2.7	0.34480	2.9	0.05228	1.1	0.93	301	8	301	8	298	25	101
A44	66,334	8049	323	0.004	1.1	0.04315	2.6	0.30950	4.2	0.05202	3.3	0.61	272	7	274	10	286	76	95
A45	53,102	6735	297	0.001	0.2	0.04824	2.7	0.34540	3.2	0.05193	1.8	0.83	304	8	301	8	282	41	108
A48	41,021	4715	209	0.002	2.4	0.04760	2.6	0.34740	6.9	0.05293	6.4	0.38	300	8	303	18	326	146	92
A53	108,805	12,507	564	0.005	1.5	0.04791	2.6	0.34790	4.3	0.05266	3.4	0.61	302	8	303	11	314	77	96
A54	57,794	7324	312	0.004	0.8	0.04627	2.8	0.32530	3.7	0.05100	2.4	0.76	292	8	286	9	241	55	121
A56	18,717	2409	99	0.001	0.3	0.04492	2.7	0.31850	3.3	0.05143	2.0	0.79	283	7	281	8	260	47	109
A57	23,856	2788	124	0.004	0.8	0.04774	2.6	0.34390	3.6	0.05224	2.5	0.73	301	8	300	9	296	57	102
A62	58,937	7413	318	0.004	0.4	0.04672	2.6	0.33630	3.1	0.05221	1.7	0.84	294	8	294	8	294	38	100
A63	55,029	7326	322	0.002	0.1	0.04810	2.7	0.34790	3.0	0.05246	1.3	0.91	303	8	303	8	305	29	99
A64	81,550	10,757	448	0.002	0.4	0.04541	2.7	0.32830	3.2	0.05243	1.7	0.85	286	8	288	8	304	38	94
A65	90,210	11,246	442	0.007	1.4	0.04175	3.5	0.30170	4.9	0.05241	3.5	0.71	264	9	268	12	303	79	87
A66	22,750	3021	132	0.004	0.1	0.04801	2.9	0.34490	3.2	0.05211	1.4	0.90	302	9	301	8	290	33	104
A80	107,614	12,509	547	0.003	1.5	0.04665	2.5	0.33680	4.3	0.05236	3.5	0.58	294	7	295	11	301	80	98
zr2 secondary zircon																			
A08	190,575	18,186	461	0.015	1.4	0.02322	3.7	0.1651	4.9	0.05155	3.1	0.76	148	5	155	7	265	72	56
A10	117,548	11,656	387	0.019	1.9	0.03282	3.0	0.2383	4.5	0.05265	3.4	0.67	208	6	217	9	314	76	66
A11	47,795	4670	195	0.006	1.9	0.04363	2.8	0.3184	5.0	0.05293	4.2	0.55	275	7	281	12	326	95	85

Table 2 (continued)

Grain	207Pb[a] (cps)	U[b] (ppm)	Pb[b] (ppm)	Th/U[b]	206Pbc[c] (%)	206Pb/238U[d]	±2σ (%)	207Pb/235U[d]	±2σ (%)	207Pb/206Pb[d]	±2σ (%)	rho[e]	206Pb/238U (Ma)	±2σ (Ma)	207Pb/235U (Ma)	±2σ (Ma)	207Pb/206Pb (Ma)	±2σ (Ma)	conc.[f] (%)
A13	178,120	31,016	652	0.014	3.5	0.02120	3.7	0.1499	7.3	0.05128	6.3	0.50	135	5	142	10	253	146	53
A15	19,854	5285	209	0.002	0.8	0.04298	2.7	0.3065	3.6	0.05172	2.3	0.76	271	7	271	9	273	54	99
A17	168,406	13,221	498	0.017	2.3	0.03577	2.7	0.2601	5.1	0.05274	4.4	0.53	227	6	235	11	317	99	71
A18	193,183	18,911	663	0.017	2.1	0.03396	2.5	0.2382	4.7	0.05088	4.0	0.53	215	5	217	9	236	92	91
A20	175,536	27,332	852	0.010	3.3	0.03226	3.9	0.2281	7.4	0.05127	6.2	0.53	205	8	209	14	253	144	81
A23	69,357	6352	269	0.012	0.8	0.04346	2.6	0.3089	3.1	0.05156	1.8	0.82	274	7	273	8	266	41	103
A25	152,042	20,320	568	0.013	1.3	0.02841	6.2	0.1998	6.9	0.05102	3.1	0.90	181	11	185	12	242	71	75
A27	24,702	2803	119	0.005	1.2	0.04545	2.8	0.3285	4.1	0.05242	3.0	0.69	287	8	288	10	304	67	94
A28	118,495	13,590	570	0.015	4.2	0.04269	3.1	0.3093	7.5	0.05255	6.8	0.41	269	8	274	18	309	155	87
A30	37,963	3667	135	0.004	0.5	0.03982	3.7	0.2894	4.1	0.05271	1.8	0.90	252	9	258	9	316	41	80
A42	302,716	33,669	713	0.004	9.2	0.01915	13.4	0.1454	17.3	0.05507	10.9	0.77	122	16	138	22	415	244	29
A46	129,615	17,921	349	0.010	3.4	0.01919	8.7	0.1374	11.0	0.05192	6.7	0.79	123	11	131	14	282	154	43
A47	57,395	5777	214	0.006	1.8	0.03982	8.6	0.2882	9.8	0.05250	4.6	0.88	252	21	257	22	307	106	82
A49	96,839	6634	307	0.003	2.4	0.04434	3.1	0.3186	5.1	0.05212	4.0	0.62	280	9	281	13	291	91	96
A50	24,275	3320	138	0.003	0.2	0.04560	3.0	0.3288	3.7	0.05230	2.0	0.83	287	9	289	9	298	46	96
A51	18,928	2152	86	0.004	0.1	0.04345	2.5	0.3119	2.8	0.05206	1.2	0.90	274	7	276	7	288	28	95
A52	34,759	4742	197	0.003	0.1	0.04536	2.7	0.3254	3.0	0.05203	1.2	0.91	286	8	286	7	287	28	100
A55	85,102	6071	289	0.022	5.2	0.04686	3.2	0.3347	9.3	0.05180	8.7	0.35	295	9	293	24	277	199	107
A58	84,752	10,582	362	0.009	0.7	0.03680	7.4	0.2602	7.7	0.05128	2.1	0.96	233	17	235	16	253	48	92
A59	78,444	10,256	436	0.001	0.3	0.04637	2.8	0.336	3.2	0.05256	1.4	0.89	292	8	294	8	310	33	94
A60	70,836	7625	279	0.011	2.4	0.03791	4.2	0.2751	6.5	0.05264	5.0	0.64	240	10	247	14	313	113	77
A61	136,725	23,586	627	0.004	2.4	0.02779	22.0	0.2009	22.8	0.05244	6.0	0.96	177	38	186	39	305	136	58
A72	135,308	14,800	570	0.007	2.5	0.03983	2.5	0.2903	5.7	0.05286	5.1	0.44	252	6	259	13	323	115	78
A73	79,761	4965	237	0.069	2.3	0.04514	3.5	0.3228	5.4	0.05187	4.0	0.66	285	10	284	13	280	92	102
A74	29,020	5474	229	0.005	1.1	0.04497	3.4	0.3229	4.5	0.05208	2.9	0.76	284	9	284	11	289	66	98
A75	126,701	14,611	476	0.013	3.2	0.03295	3.0	0.2398	6.8	0.05279	6.1	0.44	209	6	218	13	320	138	65
A76	37,515	5295	195	0.003	0.4	0.03997	3.5	0.2892	3.9	0.05247	1.7	0.90	253	9	258	9	306	38	83
A77	30,580	2677	123	0.009	3.2	0.04663	3.0	0.3336	6.8	0.05189	6.2	0.43	294	9	292	18	280	141	105
A78	161,662	11,209	374	0.021	3.5	0.02870	3.6	0.2069	5.7	0.05228	4.5	0.63	182	6	191	10	298	102	61
A79	22,642	2753	119	0.005	1.0	0.04632	2.6	0.3319	3.7	0.05196	2.7	0.69	292	7	291	9	284	62	103
A81	110,982	4860	269	0.0086	11.7	0.04716	3.2	0.3344	12.4	0.05143	12.0	0.25	297	9	293	32	260	275	114
Xenotime																			
A82	18,072	4974	214	0.006	0.8	0.04635	2.8	0.3368	3.7	0.05271	2.5	0.75	292	8	295	10	316	56	92
A83	47,843	7720	370	0.055	1.4	0.04503	3.5	0.3237	4.2	0.05213	2.4	0.83	284	10	285	11	291	54	97
A84	95,322	13,731	609	0.121	0.0	0.04656	2.7	0.3358	3.0	0.05230	1.1	0.92	293	8	294	8	299	26	98
A85	113,171	16,758	726	0.040	0.0	0.04691	2.7	0.3362	3.0	0.05197	1.3	0.90	296	8	294	8	284	30	104

Table 2 (continued)

Grain	207Pb[a] (cps)	U[b] (ppm)	Pb[b] (ppm)	Th/U[b]	206Pbc[c] (%)	206Pb/238U[d]	±2σ (%)	207Pb/235U[d]	±2σ (%)	207Pb/206Pb[d]	±2σ (%)	rho[e]	206Pb/238U	±2σ (Ma)	207Pb/235U	±2σ (Ma)	207Pb/206Pb	±2σ (Ma)	conc.[f] (%)
A86	94,958	14,380	716	0.102	1.5	0.04587	3.2	0.3283	3.8	0.05191	2.1	0.84	289	9	288	10	281	48	103
A87	62,461	21,803	949	0.074	b.d.	0.04643	2.6	0.3323	2.9	0.05191	1.1	0.92	293	8	291	7	281	26	104
A88	174,450	25,349	453	0.049	1.8	0.01655	6.0	0.1192	6.9	0.05223	3.5	0.87	106	6	114	8	296	79	36
A89	124,888	22,352	983	0.047	1.6	0.04613	4.7	0.3300	5.7	0.05188	3.3	0.82	291	13	290	15	280	76	104
A90	56,918	4788	305	0.257	1.4	0.04697	2.6	0.3407	4.1	0.05262	3.2	0.63	296	7	298	11	312	72	95
Reference materials																			
Moa-cir[g]	24,660	4098	2933	24	0.35	0.08256	2.5	0.6475	3.2	0.05688	1.8	0.63	511	12	507	13	487	40	105
Man-a[g]	17,195	1888	4389	79	0.38	0.0887	2.6	0.7152	2.0	0.05849	1.2	0.77	548	14	548	8	548	26	100
Ples.[g]	19,922	850	44	0.10	0.41	0.05378	1.4	0.39506	2.2	0.05327	1.9	0.70	338	5	338	6	340	42	100
91,5-00[g]	21,120	97	18	0.30	1.46	0.17935	1.9	1.85368	2.6	0.07496	1.6	0.69	1065	18	1063	18	1067	31	100

Spot size, zircon =23 μm, xenotime =15–23 μm; depth of crater ~15 μm. ^{206}Pb/^{238}U error is the quadratic additions of the within run precision (2 SE) and the external reproducibility (2 SD) of the GJ-1 zircon. ^{207}Pb/^{206}Pb error propagation following Gerdes and Zeh (2009). ^{207}Pb/^{235}U error is the quadratic addition of the ^{207}Pb/^{206}Pb and ^{206}Pb/^{238}U uncertainty

[a] Within run background-corrected mean ^{207}Pb signal in cps (counts per second)

[b] U and Pb content and Th/U ratio were calculated relative to GJ-1 reference zircon

[c] Percentage of the common Pb on the ^{206}Pb. b.d. = below dectection limit

[d] Corrected for background, within-run Pb/U fractionation (in case of ^{206}Pb/^{238}U) and common Pb using Stacey and Kramers (1975) model Pb composition and subsequently normalised to GJ-1 (ID-TIMS value/measured value); ^{207}Pb/^{235}U calculated using ^{207}Pb/^{206}Pb/(^{238}U/^{206}Pb*1/137.88)

[e] rho is the ^{206}Pb/^{238}U/^{207}Pb/^{235}U error correlation coefficient

[f] Degree of concordance =^{206}Pb/^{238}U age / ^{207}Pb/^{206}Pb age × 100

[g] Accuracy and reproducibilty was checked by repeated analyses of reference zircon Plesovice and 91,500 (n = 5), and Moacir, Manangotry and Namaqualand monazites (n = 9); data given as mean with 2 standard deviation uncertainties. Spot size were 23–33 μm for Plesocive, 50 μm for 91,500 and 15 μm for Moacir and Manangotry monazite

pegmatites belong to type I (L7) and type III (L3). Their geographic coordinates and description are given in Table 3. Pegmatite L3 (type III) is a well-zoned pegmatite located in the cordierite-andalusite metamorphic zone. The dyke is 100 m long and 10 m wide. Pegmatite L7 (type I) is a large (200 × 20 m) homogeneous dyke emplaced in the sillimanite-K-feldspar zone.

Textural and chemical features of CGM and zircon

In type II to type IV pegmatites, columbite-group minerals occur as millimeter to centimeter-sized tabular crystals included in major mineral constituents like mica and albite (Fig. 3a) and sometimes arranged in "star shape" (Fig. 3d-e). Backscattered electron images reveal complex chemical zoning including simple progressive zoning, oscillatory zoning and patchy zoning. Bizonal crystals with broad bands showing sharp chemical contrasts between a dark Nb-rich core and a bright thin Ta-rich rim are common (Fig. 3d-e). Other Nb-Ta-minerals associated with CGM include wodginite, cassiterite and microlite. Zircon and CGM may be found intimately associated, either as intergrowth (Fig. 3b) or as inclusions (Fig. 3c). Zircon is mostly found as fine-grained (<1 mm) euhedral crystals disseminated in major silicate minerals. It can be slightly zoned with concentric bands (Fig. 3h), but radiation damage generally masks this zoning (Fig. 3i). Metamict and inclusion-rich crystals such as the ones shown in Fig. 3i-j were discarded for age dating. Zircons from the type I pegmatite L7 are coarser-grained and present complex oscillatory zoning with zones of porous inclusion-rich zircon (Fig. 3f-g); these two types of zircon zones are later distinguished as primary *versus* secondary based on their geochemistry. Xenotime occurs in direct contact with pegmatite L7 zircons. It shows resorbed textures and systematically occurs near zircon cores, which evokes exsolution during dissolution-reprecipitation of primary zircon.

CGM chemistry includes minor concentrations of TiO_2 (<1.7 wt%), WO_3 (<1.4 wt%), SnO_2 (<1 wt%), ZrO_2 (<0.5 wt%), UO_2 (<0.4 wt%) and Sc_2O_3 (<0.2 wt%). EPMA analyses show a large range of compositions (Table 4) that plot in the ferrocolumbite to ferrotantalite parts of the CGM quadrilateral (Fig. 4). Core to rim variations illustrate the common Ta over Nb enrichment that is generally observed during CGM fractionation. Nb-Ta fractionation is also visible from type II to type IV CGM, and can be illustrated in a Rayleigh-type Nb/Ta *vs.* Ta_2O_5 fractionation diagram (Fig. 5). Fe-Mn fractionation leads to a general Fe enrichment over Mn.

Zircon chemistry reveals high concentrations of UO_2 (up to 1.6 wt%), and HfO_2 concentrations ranging from 2.1 to 6.1 wt%, which slightly increase from type I to type III and IV pegmatites (Table 5). Figure 5 illustrates this Zr/Hf fractionation trend. In type I zircon from the L7 pegmatite (Fig. 3f-g), three types of zircon zones were distinguished based on backscattered images and show distinct chemistry (Table 5; see Fig. 6 for outline of zircon zones). The highly porous and inclusion-rich cores have negligible UO_2 and Y_2O_3 concentrations, whereas the oscillatory zones (zr1) have low UO_2 and Y_2O_3 concentrations (0.6 and 0.1 wt% in average). On the Zr/Hf fractionation trend (Fig. 5), these two zircon zones plot on a continuous trend which can be interpreted as magmatic fractionation. These zircon zones are therefore interpreted as primary. Alternatively, the patchy zones (zr2), which crosscut the oscillatory zones, have high UO_2 and Y_2O_3 concentrations (up to 3 and 1.9 wt% respectively) and low totals due to metamictization. They also display high levels of impurities (P, Ca and Fe). The P + Y component is negatively correlated with Zr + Hf + Si (*apfu*); its incorporation is explained by the vector $P^{5+} + Y^{3+} = Si^{4+} + Zr^{4+}$, which reflects the solid solution between zircon and xenotime (Fig. 6). This third zircon type plots outside the Zr/Hf fractionation trend and is therefore interpreted as secondary. Few EPMA analyses of xenotime revealed UO_2 and ThO_2 concentrations of 4 and 0.1 wt% in average, respectively.

U-Pb dating

Full age data is available in Table 1 (pegmatite L3) and Table 2 (pegmatite L7). Table 6 summarizes the number of grains that were analyzed, the total number of analyses and the number of analyses that were used to calculate Concordia ages. Concordia ages are given except when they are too few, in this case intercept ages are given.

For pegmatite L3 (type III), U-Pb analyses of zircon and CGM reported in Concordia diagrams (Fig. 7) spread over a large range of isotopic ratios along discordant lines, indicating extensive lead loss. For CGM, 6 points plot on the Concordia line and give an age of 301.9 ± 3.8 Ma ($MSWD_{C+E}$ = 1.3 with C + E = concordance + equivalence). No distinction can be made between the two main BSE zones (see laser spot locations in Fig. 3e). For zircon, only one age plots on the Concordia line but the 26 discordant ages define an upper

Table 3 Description of the two dated pegmatite localities

	GPS coord.	Pegmatite type	Rock description	Dated minerals
L3	N42°19'30" - E03°15'31"	III	Aplitic albite vein adjacent to quartz pocket in well-zoned pegmatite	Zircon and CGM
L7	N42°20'01" - E03°15'50"	I	Poorly-zoned, medium-grained, simple pegmatite with abundant garnet + tourmaline and minor sillimanite + cordierite	Zircon and xenotime

Fig. 3 BSE pictures showing
CGM inclusions within mica in
pegmatite L4 (**a**), the intimate and
cogenetic association between
CGM and zircon in pegmatite L2
(**b**) and L3 (**c**), the star-shape habit
of CGM at different scales, and its
bizonal chemical zoning in
pegmatite L2 (**d**) and L3 (**e**),
complex zoning in type-I zircon
and its association with xenotime
in pegmatite L7 (**f-g**), various
zircon habits, from slightly zoned
(**h**, pegmatite L3) to highly
metamict (**i**, pegmatite L4) and
inclusion-rich (**j**, pegmatite L5).
In Fig. 3e, laser-spot locations for
U-Pb dating are marked with
circles. ms: muscovite, zrn:
zircon, xtm: xenotime
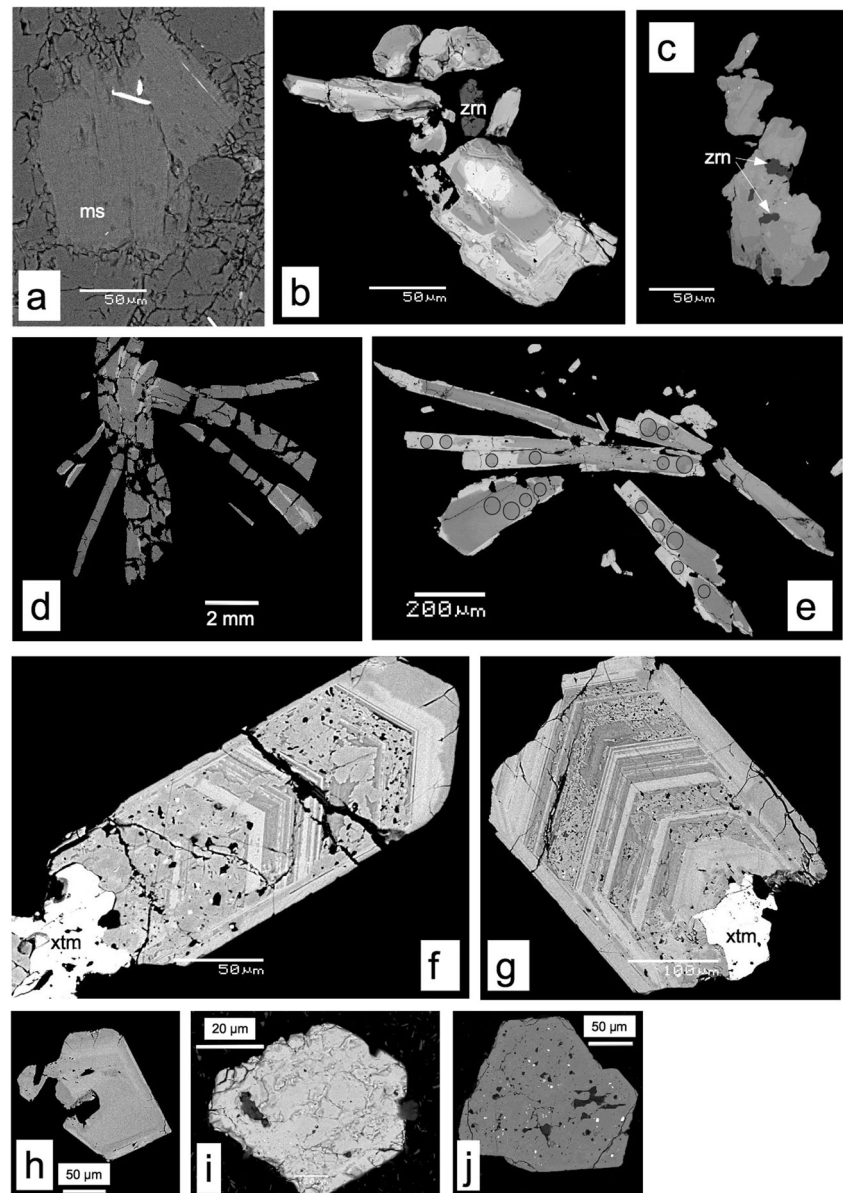
intercept at 298.7 ± 5.7 Ma (MSWD =1.5). The BSE images
of the analyzed zircon grains (Figs. 3j and 8) reveal highly
porous and inclusion-rich crystals, supporting lead loss as the
cause of the dispersion on the Discordia line. The duplicate
analyses performed in Clermont-Ferrand (inset of Fig. 7b),
indicate a combination of discordance and common Pb con-
tribution. The eight remaining concordant analyses display a
Concordia Age of 297.3 ± 2.1 Ma (MSWD$_{C+E}$ = 1.6, n = 8). A
second, smaller group of concordant analyses displays a youn-
ger age (*ca.* 275 Ma).

In pegmatite L7 (type I), oscillatory-zoned (primary, zr1 in
Fig. 6) and porous (secondary, zr2 in Fig. 6) zones of zircon
were thoroughly distinguished during laser spot
location (Fig. 9), and the age results display two age groups
(Fig. 10). In primary zircon (zr1), 19 of the 28 U-Pb ages plot

on the Concordia and display an age of 296.2 ± 2.5 Ma
(MSWD$_{C+E}$ = 1.7, n = 19). For secondary zircon (zr2), the 36
analyses are spread over a large range of isotopic ratios and 12 of
them plot on the Concordia line and give an age of
290.5 ± 2.5 Ma (MSWD$_{C+E}$ = 0.7). Eight of the 12 xenotime
U-Pb analyses plot on the Concordia and display an age of
292.9 ± 2.9 Ma (MSWD$_{C+E}$ = 0.76).

Discussion

Columbite versus zircon dating

In-situ U-Pb geochronology by LA-ICPMS on columbite-
group minerals has been developed in the 2000s (Smith et al.

Table 4 Chemical compositions of columbite-group minerals as determined by EPMA and structural formulae calculated for 6 oxygens

	Type II Columbite	Type III Columbite	Type III Tantalite	Type IV Tantalite
N	24	454	70	35
wt%				
Ta_2O_5	19.09	25.57	54.93	47.04
Nb_2O_5	63.62	56.09	27.28	34.06
TiO_2	0.52	0.62	0.86	0.40
SnO_2	0.03	0.29	0.35	0.17
WO_3	0.14	0.28	0.23	n.a.
UO_2	0.05	0.05	0.05	0.05
ZrO_2	*bdl*	0.02	0.03	*bdl*
PbO	*bdl*	0.01	0.04	*bdl*
ThO_2	*bdl*	0.03	0.02	*n.a.*
Sc_2O_3	0.03	0.04	0.10	*n.a.*
FeO	11.56	12.28	11.29	12.69
MnO	7.73	6.26	4.77	4.74
Total[a]	102.78	101.54	99.95	99.17
Structural formula for 6O				
Ta^{5+}	0.31	0.43	1.07	0.89
Nb^{5+}	1.69	1.55	0.88	1.07
Ti^{4+}	0.02	0.03	0.05	0.02
Sn^{4+}	0.001	0.007	0.006	0.005
Total site B	2.02	2.02	2.01	1.99
Fe^{2+}	0.57	0.63	0.68	0.74
Mn^{2+}	0.38	0.33	0.29	0.28
Sc^{3+}	0.002	0.007	0.010	
Total site A	0.95	0.96	0.98	1.02

bdl below detection limit (0.02 wt% ZrO_2 and ThO_2, 0.01 wt% PbO)

N number of analyses, *n.a.* not analyzed

[a] High totals on Nb-rich CGM are due to analytical problems on Nb

2004) and is now widely applied for pegmatite age determination (Melcher et al. 2008, 2015; Dewaele et al. 2011; Melleton et al. 2012; Deng et al. 2013). However, most geochronological studies have used zircon standardization, arguing that matrix-dependent effects are low (Melcher et al. 2008). Some of these geochronological results are Precambrian in age, and are therefore less sensitive to U/Pb fractionation. Che et al. (2015a, b) recently evaluated the effect of matrix-dependent fractionation by comparing U-Pb ages obtained on CGM using two different references (Zircon 91,500 and Coltan 139), and noticed a significant matrix effect leading to approximately 7–15 % younger ages where zircon references were used compared to the CGM reference. In our study, CGM ages were obtained using zircon GJ-1 primary reference and Coltan 139 was only used as a secondary control reference, therefore the Concordia age of 301.9 ± 3.8 Ma may be slightly shifted on the Concordia, which may explain the slight difference between that age and the zircon Concordia age of 297.3 ± 2.1 Ma obtained in the same sample. However, the two ages are coeval within error, and the reliability of the CGM age is evidenced by the fact that Coltan 139 yields a correct age when normalized to GJ-1 zircon in the same analytical series (Table 1).

Fig. 4 Chemical variations of CGM in the columbite quadrilateral. *Arrows* indicate core to rim variations in single samples

Fig. 5 Rayleigh fractionation trends for zircon and CGM of the different pegmatite types
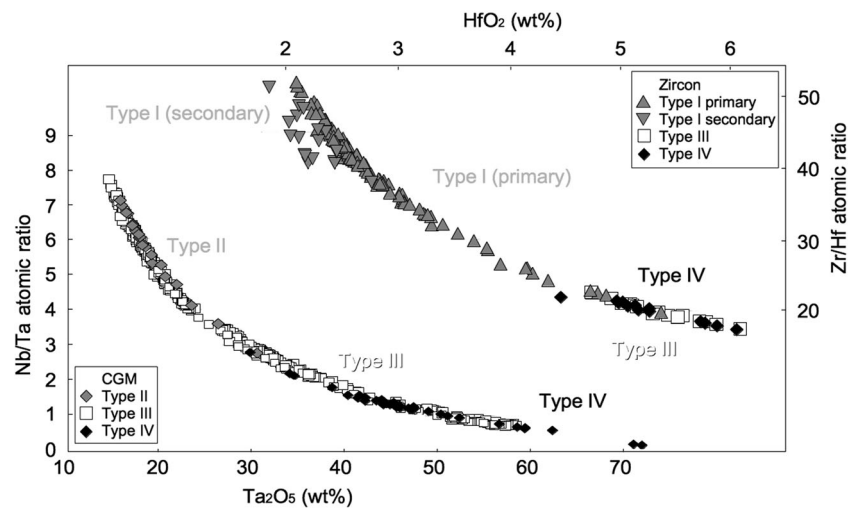
Dating pegmatite emplacement

The primary magmatic origin of CGM and zircon dated at *c.* 299 Ma is evidenced by several indicators. Textural relationships between zircon, CGM and major silicate minerals (feldspars, muscovite or garnet) indicate that zircon and CGM are cogenetic and crystallized at the pegmatitic stage. The patchy zones in L7 zircon (Figs. 3f-g and 6) are an exception; they are interpreted as secondary post-solidus phases. In CGM, the sharp chemical contrast between Nb-rich cores and Ta-rich rims is not reflected by a detectable change in their ages. In pegmatite L7 (type I) zircon, the porous and inclusion-rich cores have similar chemistry compared to primary magmatic oscillatory-zoned zircon (Fig. 6), which reflects their

pegmatitic origin instead of being inherited cores. Generally, the high Zr (and HFSE in general) solubilities in F-Li-P-rich pegmatitic melts (Linnen 1998) lower the chances to find inherited zircon cores in pegmatites. Consequently, it can be stated with high confidence that the obtained zircon and CGM ages dated at *c.* 299 Ma are representative of the pegmatite emplacement. The parallel trends followed by the Zr/Hf and Nb/Ta Rayleigh fractionation curves (Fig. 5) are also evidences that CGM and zircon both followed magmatic fractionation trends and therefore crystallized together at the magmatic stage (Hulsbosch et al. 2014).

The different zones of pegmatite L7 (type I) zircon reflect several crystallization stages. Oscillatory-zoned zircon may have crystallized at magmatic stages, whereas the patchy

Table 5   Chemical compositions of zircon as determined by EPMA

Label	L5	L7-cores	L7-zr1	L7-zr2	L3	L4
Type	I	I	I	I	III	IV
N	*15*	*8*	*82*	*24*	*17*	*13*
wt%						
SiO_2	31.38	32.02	31.71	28.29	30.88	30.71
ZrO_2	63.28	63.83	63.32	58.14	62.18	61.47
HfO_2	4.03	3.17	2.62	2.25	5.33	5.30
P_2O_5	0.15	0.25	0.50	2.22	0.08	0.14
CaO	0.02	0.01	0.01	0.24	0.03	0.04
FeO	0.17	0.16	0.16	0.97	0.05	1.16
Y_2O_3	0.06	0.00	0.09	0.96	0.05	0.06
Ce_2O_3	0.04	0.02	0.03	0.03	0.05	0.04
Ta_2O_5	0.12	*n.a.*	*n.a.*	*n.a.*	0.18	0.14
PbO_2	0.14	*n.a.*	*n.a.*	*n.a.*	0.11	0.11
UO_2	0.78	0.04	0.60	1.51	0.69	0.74
ThO_2	*n.a.*	0.10	0.06	0.07	*n.a.*	*n.a.*
Total	99.53	99.62	99.11	95.09	99.31	98.84

N number of analyses, *n.a.* not analyzed
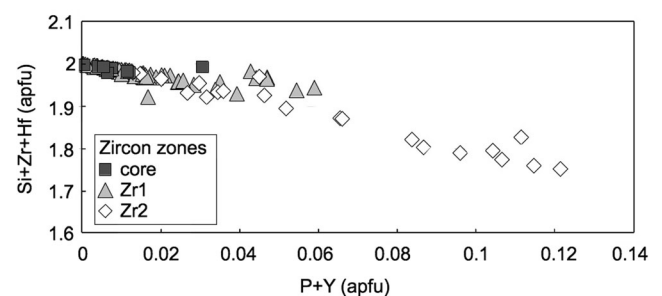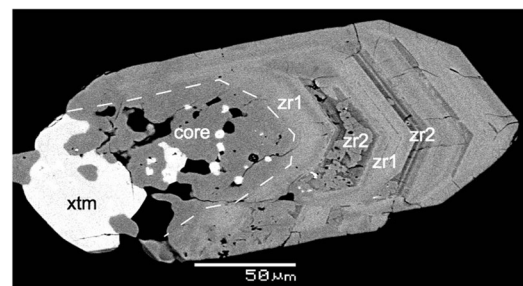
Fig. 6 BSE picture of a zircon crystal (pegmatite L7) showing an inclusion-rich core, oscillatory-zoned primary zircon (zr1) and patchy-zoned secondary zircon (zr2), as well as xenotime (xtm). The graph shows Si + Zr + Hf vs. P + Y apfu contents for the different zircon zones

Table 6 Synthesized age data

Pegmatite	Mineral	N1	N2	Mineral characteristics	Crystal size (μm)	[U] (ppm)	[Pb] (ppm)	Reference material	Age	C or I[a]
L3	Zrn	26	17	Euhedral zoned crystals	200	3000–30,000	50–600	zircon	298.7 ± 5.7	I [1]
	CGM	34	3	Needle-shaped zoned crystals	500	60–400	2–20	CGM	301.9 ± 3.8	C [6]
L7	Zrn (zr1)	28	28	Oscillatory-zoned crystals	500	2000–15,000	100–600	zircon	296.2 ± 2.5	C [19]
	Zrn (zr2)	36	36	Porous patchy zones	200	2000–34,000	100–900	zircon	290.5 ± 2.5	C [12]
	Xenotime	12	9	Anhedral grains overgrown on zircon	100	5000–25,000	200–1000	titanite	292.9 ± 2.9	C [8]

Errors are given as 2σ

N1 total number of analyses, *N2* number of analyzed grains

[a] C or I – age determined by Concordia (C) or Intercept (I). In brackets are the number of analyses that plot on the Concordia

zones, which crosscut the oscillatory zones (see Fig. 3f), could represent a secondary either magmatic or hydrothermal stage
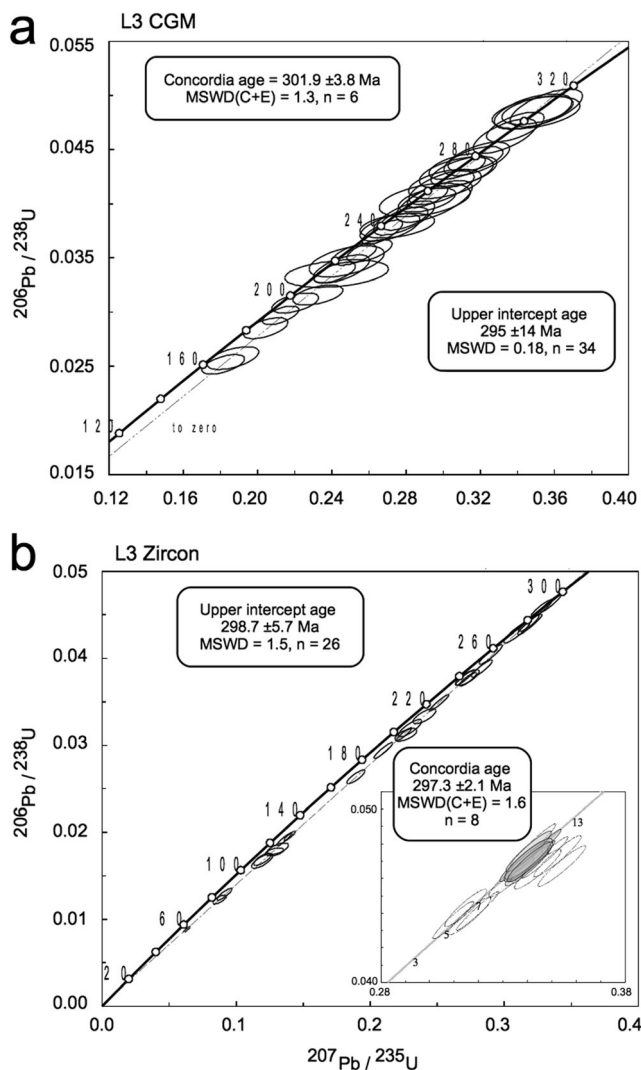
Fig. 7 U-Pb data in Concordia diagrams for L3 CGM and zircon. The *inset* of b) shows duplicate ages from LMV Clermont-Ferrand. Data-point error ellipses are 2σ

of crystallization. The highly porous nature of patchy zircon zones suggests a replacement texture, whereas its elevated U content indicates that it is strongly metamict. Such patchy textures could also be the result of the metamictization and alteration of the most U-rich zircon bands in the oscillatory zoning, as previously shown by Paquette et al. (2003), which would explain that the patchy zones follow the growth banding of magmatic zircon. In the Zr/Hf fractionation trend (Fig. 5), patchy zircon plots outside the Rayleigh trend at high Zr/Hf ratios, suggesting a non-magmatic origin, whereas all other zircon zones plot on a continuous Rayleigh curve typical of magmatic fractionation. The cores are also highly porous and inclusion-rich, and may represent primary zircon which has undergone dissolution-reprecipitation processes with ex-solution of its U and Y contents during the secondary event. The high Y + P concentrations of patchy zircon, negatively correlated with Zr + Hf + Si, suggest an important xenotime component, therefore implying that patchy zircon and xenotime are co-genetic. Whereas limited amounts of Y were integrated in primary magmatic zircon, Y was probably added by fluids during post-solidus alteration, and precipitated as Y-rich secondary zircon and xenotime replacing and overgrowing primary zircon. An alternative explanation is that xenotime was a primary magmatic phase like oscillatory-zoned zircon and it was dissolved and recrystallized during the hydrothermal event, with some Y being remobilized and integrated into secondary zircon. The U/Pb ratio of xenotime therefore dates the hydrothermal event. The slight age difference between primary (296.2 ± 2.5 Ma) and secondary (290.5 ± 2.5 Ma) zircon and its associated xenotime (292.9 ± 2.9 Ma) suggests that the secondary (hydrothermal?) event took place after pegmatite emplacement.

Implications for the geochronology of late Variscan tectonics

The five obtained ages define two groups of statistically distinct ages that lie between 296 and 302 Ma for the first, and

Fig. 8 Laser spot locations for U-Pb dating in pegmatite L3 zircon. Backscattered electron images. The 100 μm scale bar is valid for all pictures
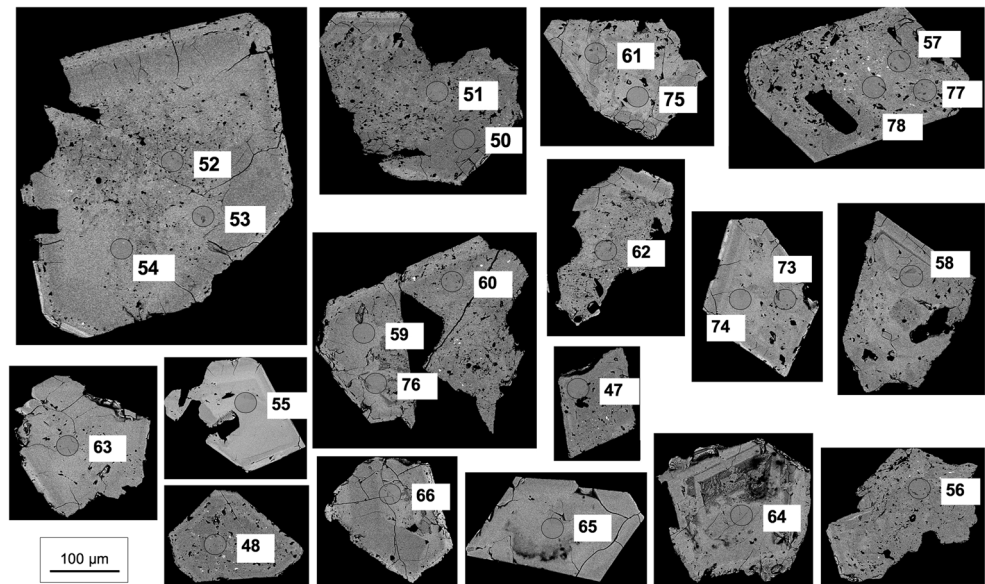
290 and 293 Ma for the second (Fig. 11). Despite their small overlap when 2-sigma error bars are considered, the two age groups remain distinct. These results have important implications for the geochronology of late Variscan tectonic events in the Cap de Creus. In a recent paper, Druguet et al. (2014) obtained similar results on syntectonic quartz diorite from the Tudela migmatitic complex, dated at 298.8 ± 3.8 Ma, and granodiorite from the Roses pluton, dated at 290.8 ± 2.9 Ma (U-Pb zircon geochronology using SHRIMP). They concluded that the D3 ductile deformation extended into the Lower Permian as a transitional stage between the Variscan and Cimmerian cycles. Taking their age results and error bars into account, mean values of 298.9 ± 6 Ma and 292.4 ± 4 Ma are calculated for the two age groups (Fig. 11). The 298.9 Ma age corresponds to the emplacement and primary crystallization of the pegmatitic melts, regardless of type I or III, and is coeval with migmatization. The 292.4 Ma age correlates with zircon replacement and xenotime crystallization as a consequence of late hydrothermal reactions that affected the pegmatites after their crystallization. However, no other evidence of this late hydrothermal event was observed in our study, and its correlation with the granodiorite emplacement remains very hypothetic.

The pegmatites were emplaced near the peak of metamorphism, therefore the pegmatite age is contemporaneous or slightly younger than this metamorphic peak. Type I to type III pegmatites, were emplaced in the same time span, around 299 Ma. The high standard deviations on in-situ U-Pb geochronological methods do not permit the different pegmatitic pulses to be distinguished, although field evidences (early, syn and late D2 emplacement) support a multiple-emplacement

history for the pegmatites. Alfonso et al. (1995) report columbite-tantalite crystals showing primary, pre-deformation oscillatory zoning broken during the deformation and subsequently overgrown by a "post-tectonic" Ta-rich rim. Field structural data indicate that the pegmatites are syntectonic with D2 and are affected by (and therefore predate) D3. The idea that this late deformation event could have occurred after the Carboniferous-Permian limit, concomitant with the hydrothermal event at the origin of zircon and xenotime recrystallization dated at *c.* 292 Ma, has to be further investigated.

Although the relationship between D2 and D3 deformations has been extensively investigated (Druguet 2001; Carreras et al. 2004), the lower geochronological limit for the Variscan tectonic event remains unclear. After Laumonier et al. (2015), this orogeny extended from Namurian to Stephanian times (*c.* 325–300 Ma) in the Pyrenees. However, the latest published data (Druguet et al. 2014) and our geochronological results indicate that the upper limit of the Variscan orogeny in Cap de Creus extended into the Early Permian. In this area, the granitoids and magmatic rocks are clearly syntectonic (syn- to late-D2 and pre-D3), and dated at c. 299 and 291 Ma (Late Carboniferous and Early Permian) by Druguet et al. (2014). Druguet et al. (2014) dated the migmatization event at *c.* 299 Ma based on field structural relationships that indicate that the dated quartz dioritic magmas are synchronous with migmatites, in agreement with field relationships. Although the migmatites themselves only present inherited zircons with Precambrian ages (542 Ma at the earliest), strong field evidences in Cap de Creus and elsewhere in the Pyrenees indicate that they are Variscan. In the Pyrenees, a few granites were dated between 292 and 300 Ma

Fig. 9 Laser spot locations for U-Pb dating of pegmatite L7 zircon. Backscattered electron images. The 100 μm scale bar is valid for all pictures
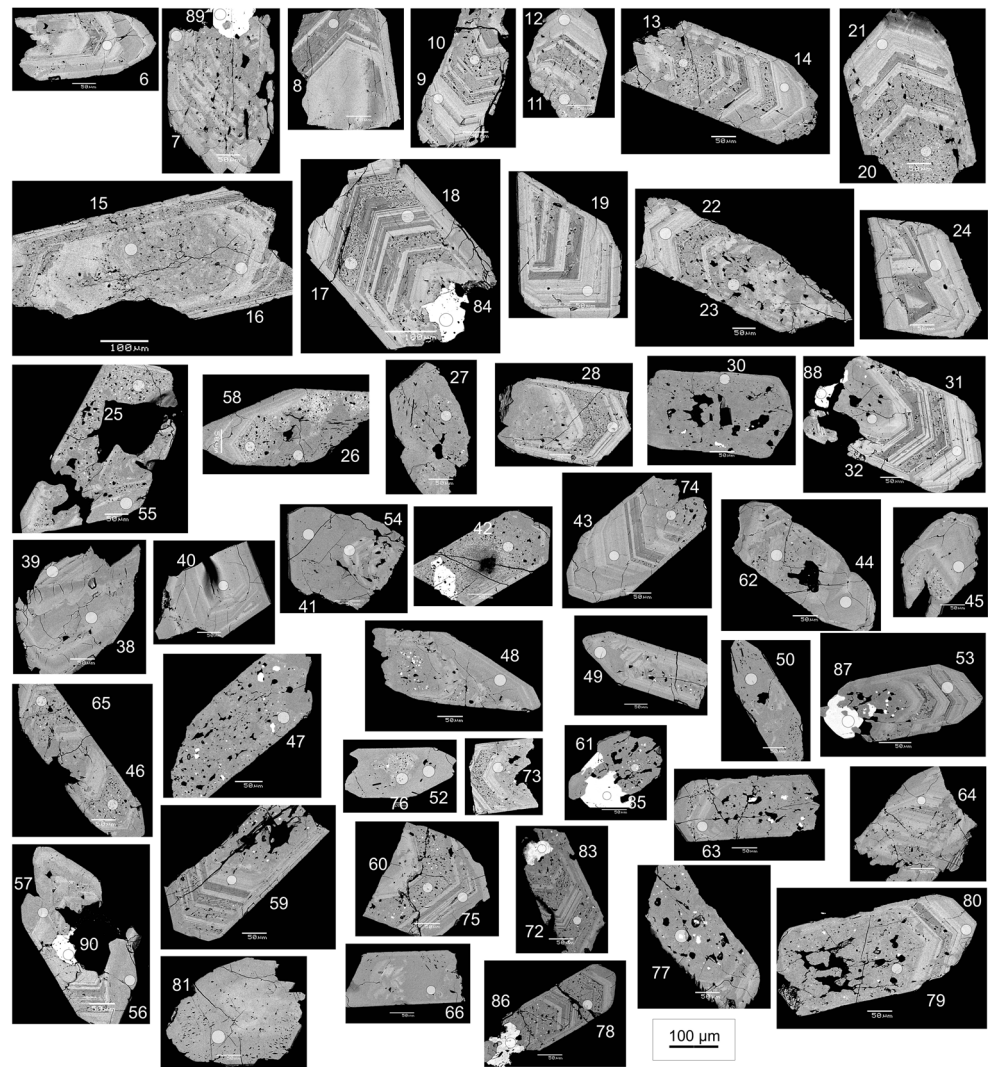
(e.g., 298.5 ± 1.8 Ma for a syn-D2 leucogranite from the Albera massif, using Th-U-Pb geochronology on monazite by electron probe microanalysis, Laumonier et al. 2015). Our geochronological results, yielding two distinct age groups at *c.* 299 and 292 Ma, suggest that the last stages of the magmatic events in the Variscan Pyrenees could have extended into the Early Permian.

The anatectic vs. granitic origin of pegmatites

The anatectic (melting of country rock) *versus* granitic (extreme fractionation of granitic melt) origin of pegmatites is still strongly debated (see London 2008 for a synthetic view of this topic), especially in cases where no potential parental granite is observed and the pegmatites are associated with migmatites, which is the case in Cap de Creus. The distribution of the pegmatites and their fractionation trends indicate an origin by differentiation of a granitic melt originating from the north of the peninsula, whereas their spatial association with migmatites has been used to argue for an anatectic origin. The common absence of visible granite in the vicinity of granitic pegmatites is generally explained by the extreme mobility and the low solidus temperatures of the highly-fluxed melts that can travel through considerable distances before the onset of dyke crystallization (Baker 1998). In general, pegmatites showing a zoned distribution with increasing fractionation degrees and mineralogical complexity are classically interpreted as being genetically related to a single melt source which evolved with fractional crystallization (London 2008). Arguments for a granitic origin of the Cap de Creus pegmatites are 1) their zonal distribution with sterile bodies located near the zone of maximum deformation in the high metamorphic zones, and fractionation degree increasing when moving toward the south down
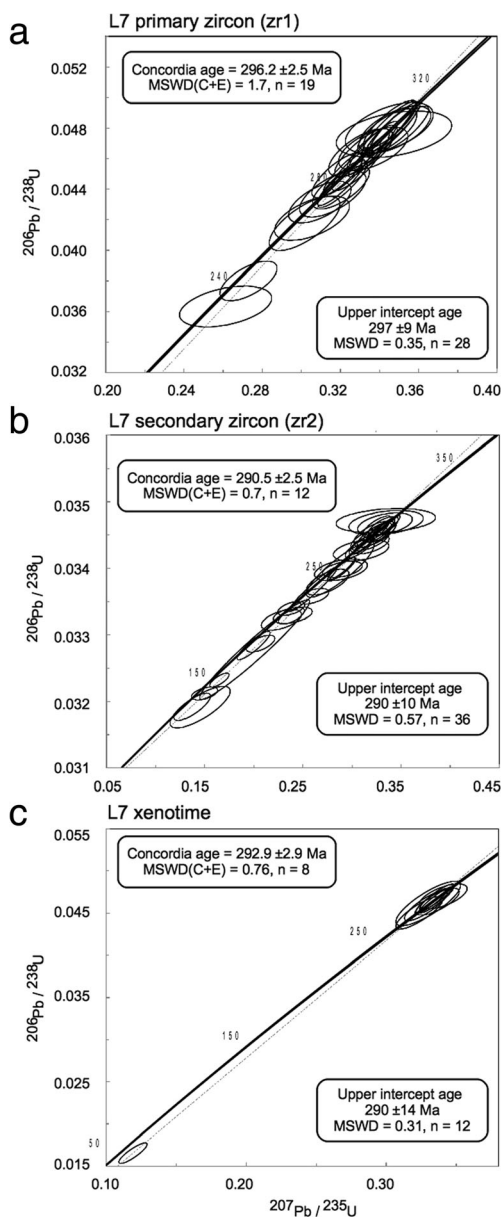
Fig. 10 U-Pb concordia diagrams for pegmatite L7 primary zircon, secondary zircon and xenotime. Data-point error ellipses are 2σ

the metamorphic gradients, and 2) progressive geochemical trends in feldspar, micas (Alfonso et al. 2003), and in Nb-Ta oxides (Alfonso et al. 1995) from type I to type IV pegmatites. The source granite could have been emplaced during the main deformation event in the migmatized area, and would now be hidden further to the north of the peninsula, or translated to the southeast by late dextral shear zones.

Arguments for the anatectic origin are provided by stable isotope constraints (Damm et al. 1992). The authors conclude that the pegmatites are derived from anatexis of the metapelitic rocks at shallow crustal levels, but their

study only takes into consideration the type I pegmatites near the lighthouse of Cap de Creus. In the Albera massif about 50 km northwest of the Cap de Creus peninsula, the peraluminous granites were interpreted as anatectic by Autran et al. (1970). Several hundred pegmatite dykes occur concentrically and zonally around muscovite-biotite granite stocks, close to their boundaries with the Precambrian orthogneisses and the Paleozoic series, therefore Autran et al. (1970) suggested an anatectic origin for the pegmatites as well. However, Malló et al. (1995) argue for an origin by magmatic fractionation of the Albera pegmatites based on the geochemical trends of the accessory minerals (phosphates and Nb-Ta-oxides). Malló et al. (1995) specify that the pegmatite source would be the anatectic muscovite-biotite leucogranites. The pegmatites in the Albera massif and in the Cap de Creus peninsula are comparable in their structure, mineralogy, geochemistry and regional distribution, which suggests a common origin.

The high fractionation degrees and highly mineralized nature of type III and IV pegmatites suggest an origin by extreme magmatic fractionation rather than *in situ* partial melting. Arguments are provided by the experimental work of London and Evensen (2002) and Evensen and London (2002) that shows taking the example of Be, that beryl saturation in pegmatites only occurs after extended crystal fractionation of large magma batches (>95 % crystallization), themselves originating from low partial melting of a fertile sedimentary source. Moreover, the continuous fractionation trends displayed by zircon and CGM indicate a genetic affiliation between all Cap de Creus pegmatites. However, this does not preclude that type I pegmatites, which are unmineralized and would be better named as pegmatitic granite, could be anatectic in origin. The large pockets of that pegmatitic granite observed in the north of the peninsula could have resulted from the partial melting of high-grade schists concomitant to the development of the migmatitic complexes. Their differentiation could have produced evolved pegmatitic melts that migrated down the metamorphic gradient and crystallized up to 3 km away from their source (Fig. 1). However, the presence of peraluminous granites associated with pegmatites in the Albera massif, also dated around 299 Ma (298.5 ± 1.8 Ma for a leucogranite, Laumonier et al. 2015), suggests that a peraluminous granite could also be the source of the Cap de Creus pegmatites. Therefore, to confirm one or the other model, geochemical and isotopic signatures of the migmatites, unmelted sedimentary units, granitic intrusives and pegmatites are necessary. 3D modeling of the pegmatite batch distribution in relation to the structural context of emplacement may also help quantifying the magma volumes implied in anatexy *versus* granitic fractionation (Demartis et al. 2011; Deveaud et al. 2013).
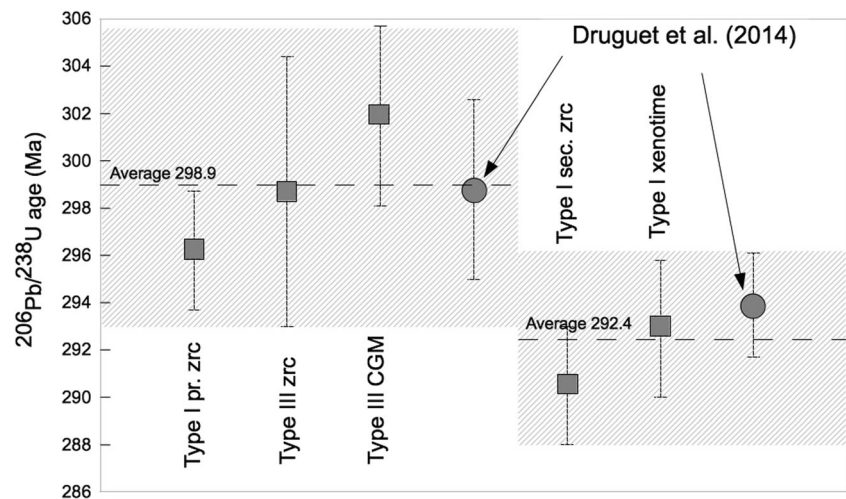
Conclusion

The U-Pb dating of magmatic zircon and columbite-group minerals in the Cap de Creus reveals that at least pegmatite types I and III were emplaced at *c.* 299 Ma. Although field relations clearly show that the various pegmatite types are not all simultaneously emplaced, our data demonstrate that they were formed and emplaced during the latest stages of the Variscan orogeny, more or less synchronously with the D2 deformation event and the associated thermal peak. Secondary zircon and xenotime that probably formed during a late post-solidus hydrothermal event, were dated at *c.* 292 Ma. This age correlates with the intrusion of late post-D2 calc-alkaline granites. This late hydrothermal event could be related to the D3 localized deformation event that is clearly post-magmatic, which would imply that the Variscan deformation was still active during the Early Permian. However, the age of the D3 event is to date unconstrained, and correlating the hydrothermal event with the D3 deformation event on one side, and the granodiorite emplacement on the other side, remains very hypothetic because of the important overlap (considering uncertainties) between the different ages.

Our results are in agreement with recent geochronological results from granitic rocks in the Variscan Eastern Pyrenees, which show that the peak of magmatic activity is well dated around 306 Ma. The pegmatitic melts were also generated simultaneously with the partial melting of the metasediments in high-grade metamorphic zones, but the extremely fractionated character of the most evolved pegmatite types III and IV suggests an origin by extreme magmatic fractionation rather than *in situ* partial melting. An alternative model would be that the most evolved pegmatitic melts could have originated from the extreme fractionation of low volumes of anatectic melts, but the presence of peraluminous granites associated with pegmatites in the Albera region, also dated at 298.5 Ma, is an evidence that peraluminous magmatism was active at that time in the area, and therefore suggests that a peraluminous granite could be the source of the most evolved Cap de Creus pegmatites.

References

Aguilar C, Montserrat L, Castiñeiras P, Navidad M (2014) Late Variscan metamorphic and magmatic evolution in the eastern Pyrenees revealed by U–Pb age zircon dating. J Geol Soc Lond 171:181–192

Alfonso P, Melgarejo JC (2008) Fluid evolution in the zoned rare-element pegmatite field at Cap de Creus, Catalonia, Spain. Can Mineral 46:597–617

Alfonso P, Corbella M, Melgarejo JC (1995) Nb–Ta minerals from the Cap de Creus pegmatite field, eastern Pyrenees: distribution and geochemical trends. Mineral Petrol 55:53–69

Alfonso P, Melgarejo JC, Yusta I, Velasco F (2003) Geochemistry of feldspars and muscovite in granitic pegmatite from the Cap de Creus field, Catalonia, Spain. Can Mineral 41:103–116

Autran A, Fonteilles M, Guitard G (1970) Relations entre les intrusions de granitoïdes, l'anatexie et le métamorphisme régional, considérées principalement du point de vue du rôle de l'eau: cas de la chaîne hercynienne de Pyrénées orientales. Bull Soc Geol Fr 7:673–731

Baker DR (1998) The escape of pegmatite dykes from granitic plutons: constraints from new models of viscosity and dike propagation. Can Mineral 36:255–263

Bons PD, Druguet E, Hamann I, Carreras J, Passchier CW (2004) Apparent boudinage in dykes. J Struct Geol 26:625–636

Carreras J (1975) Las deformaciones tardi-hercinicas en el litoral septentrional de la peninsula del Cap de Creus (prov. Gerona, España): la génesis de las bandas miloniticas. Acta Geol Hisp 10:109–115

Carreras J (2001) Zooming on Northern Cap de Creus shear zones. J Struct Geol 23:1457–1486

Carreras J, Druguet E (1994) Structural zonation as a result of inhomogeneous non-coaxial deformation and its control on syntectonic intrusions: an example from the Cap de Creus area, Eastern Pyrenees. J Struct Geol 16:1525–1534

Carreras J, Druguet E (2013) Illustrated field guide to the geology of the Cap de Creus. Servei de Publicacions de la Universitat Autònoma de Barcelona, 123 pp

Carreras J, Druguet E, Griera A, Soldevila J (2004) Strain and deformation history in a syntectonic pluton; the case of the Roses granodiorite (Cap de Creus, Eastern Pyrenees). J Geol Soc Lond Special Publications 224:307–319

Casas JM, Castiñeiras P, Navidad M, Liesa M, Carreras J (2010) New insights into Late Ordovician magmatism in the Eastern Pyrenees: U-Pb SHRIMP zircon data from the Canigó massif. Gondwana Res 17:317–324

Casas JM, Navidad M, Castiñeiras P, Liesa M, Aguilar C, Carreras J, Hofmann M, Gärtner A, Linnemann U (2015) The Late Neoproterozoic magmatism in the Ediacaran series of the Eastern Pyrenees: new ages and isotope geochemistry. Int J Earth Sci 104: 909–925

Castiñeiras P, Navidad M, Liesa M, Carreras J, Casas JM (2008) U–Pb zircon ages (SHRIMP) for Cadomian and Early Ordovician magmatism in the Eastern Pyrenees: New insights into the pre-Variscan evolution of the northern Gondwana margin. Tectonophysics 461:228–239

Černý P, Ercit TS (2005) The classification of granitic pegmatites revisited. Can Mineral 43:2005–2026

Che XD, Wu FY, Wang RC, Gerdes A, Ji WQ, Zhao ZH, Yang JH, Zhu ZY (2015a) In situ U–Pb isotopic dating of columbite–tantalite by LA–ICP–MS. Ore Geol Rev 65:979–989

Che XD, Wu FY, Wang RC, Gerdes A, Ji WQ, Zhao ZH, Yang JH, Zhu ZY (2015b) Corrigendum to "In situ U–Pb isotopic dating of columbite–tantalite by LA-ICP-MS" [Ore Geol Rev 65 (2015) 979–989]. Ore Geol Rev 67:400

Cocherie A, Baudin T, Autran A, Guerrot C, Fanning CM, Laumonier B (2005) U-Pb zircon (ID-TIMS and SHRIMP) evidence for early ordovician intrusion of metagranites in the late Proterozoic Canaveilles Group of the Pyrenees and the Montagne Noire (France). Bull Soc Geol Fr 176:269–282

Corbella M, Melgarejo JC (1993) Rare-element pegmatites of Cap de Creus Peninsula, northeast Spain: a new field of the beryl–phosphate subtype. Proc. 8th IAGOD Symp. E. Schweizerbart'sche Verlagsbuchhandlung (Nägele u. Obermiller), Stuttgart, Germany 295–302

Damm KW, Harmon RS, Heppner PM, Dornsiepen U (1992) Stable isotope constraints on the origin of the Cabo de Creus garnet-tourmaline pegmatites, Massif des Alberes, Eastern Pyrenees, Spain. Geol J 27:75–86

Demartis M, Pinotti LP, Coniglio JE, D'Eramo FJ, Tubia JM, Aragon E, Agulleiro Insua LA (2011) Ascent and emplacement of pegmatitic melts in a major reverse shear zone (Sierras de Cordoba, Argentina). J Struct Geol 33:1334–1346

Denèle Y, Laumonier B, Paquette J-L, Olivier P, Gleizes G, Barbey P (2014) Timing of granite emplacement, crustal flow and gneiss dome formation in the Variscan segment of the Pyrenees. J Geol Soc Lond Special Publications 405:265–287

Deng XD, Li JW, Zhao XF, Hu ZC, Hu H, Selby D, de Souza Z (2013) U–Pb isotope and trace element analysis of columbite-(Mn) and zircon by laser ablation ICP–MS: implications for geochronology of pegmatite and associated ore deposits. Chem Geol 344:1–11

Deveaud S, Gumiaux C, Gloaguen E, Branquet Y (2013) Spatial statistical analysis applied to rare-element LCT-type pegmatite fields: an original approach to constrain faults–pegmatites–granites relationships. J Geosci 58:163–182

Dewaele S, Henjes-Kunst F, Melcher F, Sitnikova M, Burgess R, Gerdes A, Fernández-Alonso M, De Clerq F, Muchez P, Lehmann B (2011) Late Neoproterozoic overprinting of the cassiterite and columbite – tantalite bearing pegmatites of the Gatumba area, Rwanda (Central Africa). J Afr Earth Sci 61:10–26

Druguet E (2001) Development of high thermal gradients by coeval transpression and magmatism during the Variscan orogeny: insights from the Cap de Creus (Eastern Pyrenees). Tectonophysics 332: 275–293

Druguet E, Carreras J (2006) Analogue modelling of syntectonic leucosomes in migmatitic schists. J Struct Geol 28:1734–1747

Druguet E, Hutton DHW (1998) Syntectonic anatexis and magmatism in a mid-crustal transpressional shear zone: an example from the Hercynian rocks of the eastern Pyrenees. J Struct Geol 20:905–916

Druguet E, Passchier CW, Carreras J, Victor P, denBrock S (1997) Analysis of a complex high-strain zone at Cap de Creus, Spain. Tectonophysics 280:31–45

Druguet E, Castro A, Chichorro M, Pereira F, Fernández C (2014) Zircon geochronology of intrusive rocks from Cap de Creus, Eastern Pyrenees. Geol Mag 151:1095–1114

Evensen JM, London D (2002) Experimental silicate mineral/melt partition coefficients for beryllium and the crustal Be cycle from migmatite to pegmatite. Geochim Cosmochim Acta 66:2239–2265

Fusseis F, Handy MR, Schrank C (2006) Networking of shear zones at the brittle-to-viscous transition (Cap de Creus, NE Spain). J Struct Geol 28:1228–1243

Gäbler H-E, Melcher F, Graupner T, Bahr A, Sitnikova M, Henjes-Kunst F, Oberthür T, Brätz H, Gerdes A (2011) Speeding up the analytical workflow for coltan fingerprinting by an integrated mineral liberation analysis/LA-ICP-MS approach. Geostand Geoanal Res 35: 431–448

Gerdes A, Zeh A (2006) Combined U–Pb and Hf isotope LA-(MC-)ICP-MS analyses of detrital zircons: Comparison with SHRIMP and new constraints for the provenance and age of an Armorican metasediment in Central Germany. Earth Planet Sci Lett 249:47–61

Gerdes A, Zeh A (2009) Zircon formation versus zircon alteration — New insights from combined U–Pb and Lu–Hf in-situ LA-ICP-MS analyses, and consequences for the interpretation of Archean zircon from the Central Zone of the Limpopo Belt. Chem Geol 261:230–243

Gonçalves G, Lana C, Scholz R, Buick IS, Gerdes A, Kamo SL, Corfu F, Marinho MM, Chaves A, Valeriano C, Nalini HA Jr (2016) An assessment of monazite from the Itambé pegmatite district for use as U–Pb isotope reference material for microanalysis and implications for the origin of the "Moacyr" monazite. Chem Geol 424:30–50

Horstwood MSA, Foster GL, Parrish RR, Noble SR, Nowell GM (2003) Common-Pb corrected in situ U–Pb accessory mineral geochronology by LA-MC-ICP-MS. J Anal At Spectrom 18:837–846

Hulsbosch N, Hertogen J, Dewaele S, André L, Muchez P (2014) Alkali metal and rare earth element evolution of rock-forming minerals from the Gatumba area pegmatites (Rwanda): Quantitative assessment of crystal-melt fractionation in the regional zonation of pegmatite groups. Geochim Cosmochim Acta 132:349–374

Laumonier B, Autran A, Barbey P, Cheilletz A, Baudin T, Cocherie A, Guerrot C (2004) On the non-existence of a Cadomian basement in southern France (Pyrenees, Montagne Noire): implications for the significance of the pre-Variscan (pre-Upper Ordovician) series. Bull Soc Geol Fr 175:643–655

Laumonier B, Calvet M, Autran A, Rossi P, Guennoc P (2015) Notice explicative, Carte géologique de France (1/50 000), feuille Argelès-sur-Mer-Cerbère (1097). BRGM, Orléans

Liesa M, Carreras J, Castiñeiras P, Casas JM, Navidad M, Vilà M (2011) U-Pb zircon age of Ordovician magmatism in the Albera Massif (Eastern Pyrenees). Geol Acta 9:93–101

Linnen RL (1998) The solubility of Nb-Ta-Zr-Hf-W in granitic melts with Li and Li + F: constraints for mineralization in rare metal granites and pegmatites. Econ Geol 93:1013–1025

Linnen RL, Van Lichtervelde M, Černỳ P (2012) Granitic pegmatites as sources of strategic metals. Elements 8:275–280

London D (2008) Pegmatites. Can Mineral Special Publication 10, 368 p

London D, Evensen JM (2002) Beryllium in silicic magmas and the origin of beryl-bearing pegmatites. In: Grew ES (ed) Beryllium: mineralogy, petrology, and geochemistry, Rev Mineral Geochem, vol 50. Mineral Soc Am, Chantilly, pp. 445–486

Ludwig KR (2008) Isoplot 3.6. Berkeley Geochronology Center Special Publication 4, 77 p

Malló A, Fontan F, Melgarejo JC, Mata JM (1995) The Albera zoned pegmatite field, easthern Pyrenées, France. Mineral Petrol 55:103–116

Melcher F, Sitnikova MA, Graupner T, Martin N, Oberthür T, Henjes-Kunst F, Gäbler E, Gerdes A, Brätz H, Davis DW, Dewaeles S (2008) Fingerprinting of conflict minerals: columbite- tantalite ("coltan") ores. SGA News 23(1):7–13

Melcher F, Graupner T, Gäbler HE, Sitnikova M, Henjes-Kunst F, Oberthür T, Gerdes A, Dewaele S (2015) Tantalum–(niobium–tin) mineralisation in African pegmatites and rare metal granites: Constraints from Ta–Nb oxide mineralogy, geochemistry and U–Pb geochronology. Ore Geol Rev 64:667–719

Melleton J, Gloaguen E, Frei D, Novák M, Breiter K (2012) How are the emplacement of rare-element pegmatites, regional metamorphism and magmatism interrelated in the Moldanubian domain of the Variscan Bohemian massif, Czech Republic. Can Mineral 50:1751–1773

Meyer FM, Kolb J, Sakellaris GA, Gerdes A (2006) New ages from the Mauritanides Belt: recognition of Archean IOCG mineralization at Guelb Moghrein, Mauritania. Terra Nova. 18:345–352

Millonig LJ, Gerdes A, Groat LA (2013) The effect of amphibolite facies metamorphism on the U-Th-Pb geochronology of accessory minerals from meta-carbonatites and associated meta-alkaline rocks. Chem Geol 353:199–209

Navidad M, Carreras C (1995) Pre-Hercynian magmatism in the eastern Pyrenees (Cap-de-Creus and Albera massifs) and its geodynamical setting. Geol Mijnb 74:64–74

Paquette JL, Moine B, Rakotondrazafy M (2003) ID-TIMS using the step-wise dissolution technique versus ion microprobe U-Pb dating of metamict Archean zircons from NE Madagascar. Precambrian Res 121:73–84

Paquette JL, Piro JL, Devidal JL, Bosse V, Didier A (2014) Sensitivity enhancement in LA-ICP-MS by N2 addition to carrier gas: application to radiometric dating of U-Th-bearing minerals. Agilent ICP-MS J 58:4–5

Romer RL, Wright JE (1992) U-Pb dating of columbites: a geologic tool to date magmatism and ore deposits. Geochim Cosmochim Acta 56:2137–2142

Slama J, Košler J, Condon DJ, Crowley JL, Gerdes A, Hanchar JM, Horstwood MSA, Morris GA, Nasdala L, Norberg N, Schaltegger U, Schoene B, Tubrett MN, Whitehouse MJ (2008) Plešovice zircon: a new natural standard for U–Pb and Hf isotope microanalysis. Chem Geol 249:1–35

Smith SR, Foster GL, Romer RL, Tindle AG, Kelley SP, Noble SR, Horstwood M, Breaks FW (2004) U–Pb columbite– tantalite chronology of rare-element pegmatites using TIMS and Laser Ablation-Multi collector-ICP-MS. Contrib Mineral Petrol 147:549–564

Stacey JS, Kramers JD (1975) Approximation of terrestrial lead isotope evolution by a two-stage model. Earth Planet Sc Lett 26:207–221

Tera F, Wasserburg GJ (1974) U-Th-Pb systematics on lunar rocks and inferences about lunar evolution and the age of the moon. Proc. 5th Lunar Conf., Geochim Cosmochim Acta Suppl 5:1571–1599

Wiedenbeck M, Hanchar JM, Peck WH, Sylvester P, Valley J, Whitehouse M, Kronz A, Morishita Y, Nasdala L, Fiebig J, Franchi I, Girard JP, Greenwood RC, Hinton R, Kita N, Mason PRD, Norman M, Ogasawara M, Piccoli PM, Rhede D, Satoh H, Schulz-Dobrick B, Skår Ø, Spicuzza MJ, Terada K, Tindle A, Togashi S, Vennemann T, Xie Q, Zheng YF (2005) Further characterisation of the 91500 zircon crystal. Geostand Geoanal Res 28:9–39

Zeh A, Gerdes A (2012) U-Pb and Hf isotope record of detrital zircons from gold-bearing sediments of the Pietersburg Greenstone Belt (South Africa) – Is there a common provenance with the Witwatersrand Basin. Precambrian Res 204–205:46–56